J. U. ANDERSEN, S. KJÆR ANDERSEN
AND W. M. AUGUSTYNIAK

CHANNELING OF ELECTRONS AND POSITRONS

Correspondence between Classical and Quantal Descriptions

Det Kongelige Danske Videnskabernes Selskab
Matematisk-fysiske Meddelelser **39**, 10

Kommissionær: Munksgaard
København 1977

Synopsis

Channeling of 700-keV electrons in silicon has been investigated by measurements of the large-angle scattering yield from thin single crystals as a function of incidence direction. The peaks in yield for incidence parallel to low-index planes and axes are compared mainly to calculations based upon the dynamical theory of electron diffraction. This description is reviewed in a formulation emphasizing similarity to the classical theory of channeling. The relationship between the two descriptions is discussed, and correspondence in the limit of large quantum numbers is illustrated, partly by the example of a harmonic oscillator, partly by analytical results for a simple model, derived within the WKB approximation. Estimates of the magnitude of the quantum numbers associated with the transverse motion of channeled particles are derived semiclassically from the available phase space for bound states in the transverse continuum potential, and the importance of distinguishing between axes and planes and between positive and negative particles, is pointed out. These qualitative considerations are supplemented with results of numerical calculations, based upon the classical channeling theory and the dynamical theory of electron diffraction, respectively. This comparison illustrates the transition to the classical limit for increasing projectile mass and provides a quantitative test of the correspondence criteria based on semiclassical estimates.

Printed in Denmark by Bianco Lunos Bogtrykkeri A/S. ISBN 87-7304-084-3

List of Contents

Introduction

This study of electron and positron channeling may be seen as part of a general investigation of the channeling of light particles which, during the last decade, has been performed partly at the University of Aarhus, partly at Bell Telephone Laboratories. Motivated by the strong channeling effects found for heavy particles (protons, α particles, etc.)[1,2], attemps were made to look for similar phenomena for electrons penetrating single crystals[3]. The basic features of the channeling effect for both positrons and electrons were first established by Uggerhøj in a beautiful experiment[4], where the angular distribution of electrons and positrons, emitted by ^{64}Cu embedded in a copper single crystal, were studied simultaneously. The observation of an axial dip in yield for positrons, and a peak for electrons, was in qualitative agreement with expectations based upon the theory[5] of heavy-particle channeling. The measurement was continued in order to obtain more quantitative data, and the results were found to be in fair agreement with estimates based upon classical mechanics[6].

A basic difficulty in such emission experiments is the damage due to implantation of the radioactive atoms. To avoid this problem, experiments with external beams of electrons and positrons were initiated. A measurement of the large-angle scattering yield as a function of direction for an external beam is, in principle, equivalent to a determination of the angular distribution of particles emitted from lattice sites (reversibility[5] or reciprocity[7]).

Positron channeling in gold[8] and silicon[9] was studied with an external beam. The general result was that positron channeling is adequately described by the channeling theory based upon classical mechanics, although for planar channeling some fine structure due to Bragg interference was observed.

For electrons the situation is somewhat different[10]. Owing to their negative charge, electrons penetrate readily to the atomic scattering centers in the

rows and planes. Incoherent multiple scattering will therefore be stronger than for positive particles. Furthermore, it may be seen from semiclassical phase-space estimates that the number of bound states in the transverse potential is quite large in most cases for channeled positrons, while for electrons it is considerably larger than unity only at relativistic energies.

The possibility of electron motion in bound states along rows of atoms, describable to some extent by classical mechanics, was first studied theoretically by LINDHARD[11]. In an experimental study of electron channeling in gold by UGGERHØJ et al.[12], the interest was focussed on classical aspects of axial channeling and on predictions from the classical treatment. Later the measurements have been extended[13] to higher energies and to include also planar effects and a detailed comparison to many-beam calculations. Parallel to these investigations, the measurements to be reported here of the channeling of 700-keV electrons in silicon were undertaken. Results on axial channeling were included in the discussion by UGGERHØJ et al.[12,13].

Electron channeling was approached independently on the basis of the well-established theory for the phenomena observed in electron microscopy[14]. Angular variations of the electron-backscattering yield for incidence close to a planar direction were predicted by HIRSCH et al.[15] and found experimentally by DUNCOMB[16]. In the study by HALL[17] of the effect of lattice structure on the yield of characteristic x rays, the main emphasis was on a detailed description of the thickness dependence due to inelastic scattering. Later HOWIE et al.[18] studied the emission of electrons from neutron-activated thin crystals and compared to both classical calculations and calculations based upon diffraction theory. It is a common feature of these experiments that only planar channeling has been investigated. From the point of view of diffraction theory, an axis is basically an intersection of a set of planes, and nothing much but unnecessary complications is gained by studying channeling close to an axial direction[19]. In LINDHARD's theoretical work on channeling, however, the axial case is qualitatively different from the planar case. For heavy positive particles, axial effects are stronger than planar effects and therefore, from most points of view, more interesting. Also, for electrons and positrons, the quantum numbers associated with axial effects are larger than for planar effects, and classical concepts may therefore more readily be applied to the axial case.

The attempts[4,6] mentioned earlier to relate the channeling phenomena for electrons and positrons to classical channeling theory for heavy particles were met with strong criticism. The possibility of understanding electron and positron channeling on the basis of electron-diffraction theory was first

pointed out by HOWIE[20] and later argued strongly by DE WAMES et al. in a series of publications[21]. The resulting, at times rather heated, discussion greatly stimulated the interest in channeling of light particles and, more specifically, in the problem of correspondence between classical and quantal calculations related to channeling [22–25]. For fairly recent reviews of the field, and discussions of correspondence from different points of view, we may refer to Refs. 26–28.

Correspondence between classical and quantal treatment of channeling phenomena is the main theme of the present study. It is composed of four parts. The first is a report on an experimental investigation of electron channeling in silicon, performed at Bell Telephone Laboratories in 1968. The main emphasis is on measurements of axial and planar peaks in yield of large-angle scattering. While electron microscopy is based on wave interference observed in transmission, the most interesting and useful phenomenon associated with classical channeling is the strong angular dependence of the yield of processes which require a close encounter between projectiles and target atoms.

The experimental results are compared mainly to calculations based upon the dynamical theory of electron diffraction. This theoretical description is in the second part reviewed briefly in a formulation which emphasizes similarity to the classical description of channeling. Problems related to incoherent scattering are discussed qualitatively, and examples are given of the treatment in terms of an imaginary potential and scattering into plane-wave states.

Correspondence with the classical treatment is discussed in the third part and illustrated partly by an analysis of the example of a harmonic oscillator, partly by some simple calculations based upon the WKB approximation. This general analysis is followed in the fourth part by a derivation from semiclassical phase-space arguments of estimates of the number of bound states in the transverse motion of channeled particles, leading to simple criteria for the applicability of a classical description. Differences between positive and negative particles, and also between the axial and planar cases, are discussed on the basis of two examples. The transition to the classical limit is then investigated quantitatively by a comparison of classical and quantal calculations for different electron and positron energies. At high energy, where the number of bound states becomes large owing to the increase in relativistic projectile mass, the quantal results approach the classical predictions. These are for the planar case obtained from the formalism developed for heavy positive particles[29]. For negative particles,

the axial case presents special problems, in particular concerning the applicability of results obtained from the assumption of statistical equilibrium in the transverse motion. These problems are discussed in the appendix, which contains the derivation of a classical estimate of the axial peak in yield for negative particles, based on statistical equilibrium.

I. Experimental Study of Electron Channeling in Silicon

I.1. Experimental procedure

Setup. A sketch of the experimental arrangement is shown in Fig. I.1. The electron beam, with an initial energy of 800 keV, is scattered by a 30-μm gold foil. The current of electrons transmitted through the foil into the Faraday cup is used to monitor the beam intensity. The electrons scattered by 90° lose on the average ~ 100 keV in the gold foil, leading to a final beam energy of ~ 700 keV, with a measured spread of 85-keV FWHM. The angular spread of 0.05° full width is defined by a 1-mm collimator placed immediately in front of the gold foil and a 0.4-mm collimator at the entrance to the scattering chamber.

The beam is incident on a thin silicon crystal, mounted in a goniometer with two perpendicular rotations. The scattering chamber contains three different detection systems:

(i) Annular detector for electrons scattered through ~ 10–20° by the crystal.
(ii) Movable detector ('forward detector') to scan the intensity distribution in the forward direction. Both detectors are silicon surface-barrier detectors.
(iii) Film to record photographically the angular intensity distribution in the forward direction.

Crystals. The thin crystals were prepared by etching 0.15-mm thick silicon wafers, cut perpendicular to a ⟨110⟩ direction. A thicker ring was left at the edge for support. The crystals were mounted by sandwiching them between aluminum and lucite plates with a 5-mm hole in the center. Mounting the thinner crystals was a delicate operation, after which a careful examination for wrinkles was necessary.

Results for two thicknesses are reported. From an α-particle, energy loss measurement, the thicker crystal was estimated to be 2.8 μm thick. Unfortunately the thinner crystal was broken before a similar meassurement

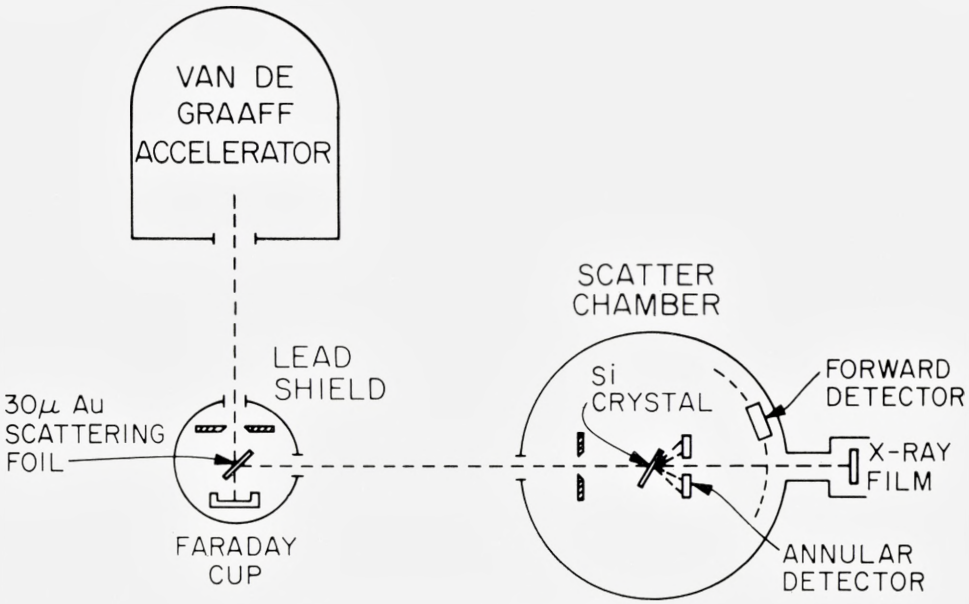

Fig. I.1: Experimental arrangement.

could be made, but from the relative electron-scattering yield, its thickness was estimated to be 0.2–0.3 μm.

Measuring procedure. The orientation of the crystal was determined by the standard technique known from proton channeling[30]. The planes were identified by an increase in yield of the scattering into the annular detector. A stereogram was constructed, and thus the rotation parameters corresponding to various planar and axial directions could be determined.

Angular scans through major planes and axes were performed by measuring the yield of scattering into the annular detector for a fixed accumulated charge in the Faraday cup. In preliminary experiments, the "forward detector" was used, positioned at some large angle to the beam direction. Strong asymmetries of the peaks in yield were observed, however, and these asymmetries turned out to be dependent on the position of the detector. Such effects are known also for proton channeling and are usually ascribed to "blocking" of the scattered particles. In this case, however, the solid angle subtended by the detector was very large compared to the widths of the channeling peaks. Also asymmetries were seen, depending only on the detector being 'to the left' or 'to the right' of the beam direction. Rather than investigate these phenomena in detail, it was decided to use an annular

counter which is axially symmetric and averages over a very large solid angle.

The forward detector was then used to scan angular distribution of the beam after its passage through the crystal. Because of the small distance from the crystal, the angular resolution was not very good. A better resolution was obtained in the photographic exposures.

I.2. Results

Results from measurements on two samples of thickness 0.2–0.3 μm and 2.8 μm, respectively, are reported. The thickness may be compared to the mean-free path for scattering, defined as $l = (N\sigma)^{-1}$, where σ is the total atomic scattering cross section and N the density of atoms, $N = 5 \times 10^{22}$ cm^{-3} for Si. A simple estimate of σ is obtained in the Born approximation for an exponentially screened Coulomb potential,

$$\sigma = \pi a^2 \varkappa^2, \tag{I.1}$$

where a is the screening parameter and $\varkappa$ is defined as

$$\varkappa = \frac{2|Z_1|Z_2 e^2}{\hbar v}. \tag{I,2}$$

Here, $Z_1 e$ and $Z_2 e$ are the charges of the particle and the scattering nucleus, and v is the particle velocity. While for $\varkappa > 1$, the collision may be described by classical mechanics[31], the Born approximation is valid in the limit of $\varkappa < 1$. In the present case, we have $\varkappa^2 \simeq 0.05$. For the screening parameter a, we way may insert the Thomas-Fermi screening radius, $a = 0.8853\ Z_2^{-1/3}\ a_0$, where a_0 is the Bohr radius, $a_0 = 0.53$ Å. This leads to a cross section of $\sigma \simeq 5 \times 10^{-3}$ Å^2 and a mean-free path for scattering, $l \simeq 4000$ Å. More accurate calculations indicate that such a simple estimate is probably not far off[32]. According to Eq. (I,1), l depends on Z_2 approximately as $l \propto Z_2^{-4/3}$ for fixed electron energy. The scattering length in gold will then be roughly ten times shorter, in good agreement with the measured value of $l \simeq 400$ Å for 1-MeV electrons[12].

Thus the thickness of the thinner sample is comparable to the scattering length, whereas the thickness of the thicker sample corresponds to about $7l$. The angular distributions of the transmitted electrons were in qualitative agreement with these estimates. For the thinner sample, the distribution consisted of an unscattered, central peak with tails due to single (or plural) scattering, whereas for the thicker sample, no central peak was observed.

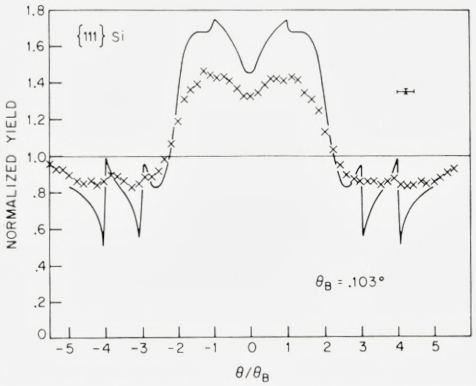

Fig. I.2: Scan through {111} plane for the 0.2–0.3-μm sample. The crosses are experimental points, and the fully drawn curve is the result of a nine-beam calculation for a static lattice. Bragg reflections of order up to ± 4 are included (9 beams).

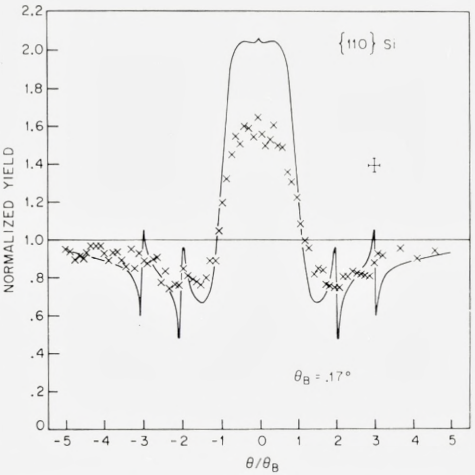

Fig. I.3: Scan through {110} plane for the 0.2–0.3-μm sample. This calculation includes reflections of order up to ± 3 (7 beams). The error flag on the upper right-hand side indicates beam divergence and statistical uncertainty of the measurements.

As mentioned above, the angular resolution in scans with the forward detector was too poor for quantitative measurements. More direct information on the scattering and its variation with incidence direction is obtained from the yield of large-angle scattering into the annular detector.

0.2–0.3 μm crystal. Scans through the three major planes, {111}, {110}, and {100} are shown in Figs. I.2–I.4. The measured yields are normalized to the yield in a "random" (nonsymmetry) direction. The angle with the plane is given in units of the Bragg angle, $\theta_B = \lambda/(2d_p)$, where λ is the electron wavelength and d_p the planar spacing. We shall discuss the calculations in more detail in the following chapter. Inelastic scattering is not included, and thus the discrepancy in peak height, due to attenuation with depth, is to be expected. If, for simplicity, exponential damping with depth is assumed, the measurements indicate that the length corresponding to a reduction by $1/e$ is approximately equal to the crystal thickness (cf. also Sec. II.7).

The general peak shapes are rather well reproduced by the calculations. For the {110} and {100} planes, the width is twice the Bragg angle, whereas for the strongest plane, the {111}, the width is 4 to 5 times θ_B. The peculiar shape of the {111} peak is due to the diamond structure of silicon. Each {111} atomic plane is split into two planes with a separation of $d_p/4$. The

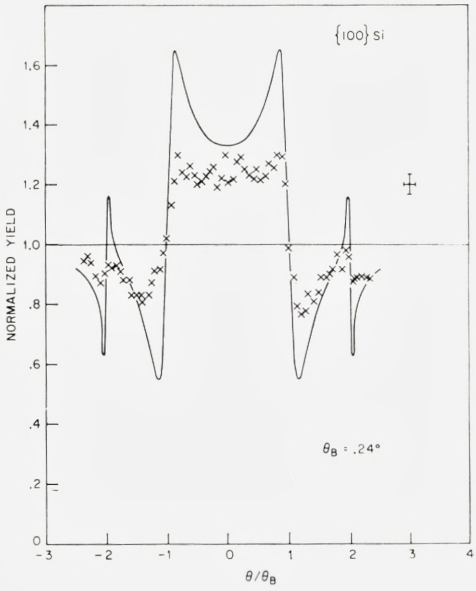

Fig. I.4: Scan through {100} plane for the 0.2–0.3-μm sample compared with five-beam calculation. The error flag on the upper right-hand side indicates beam divergence and statistical uncertainty of the measurements.

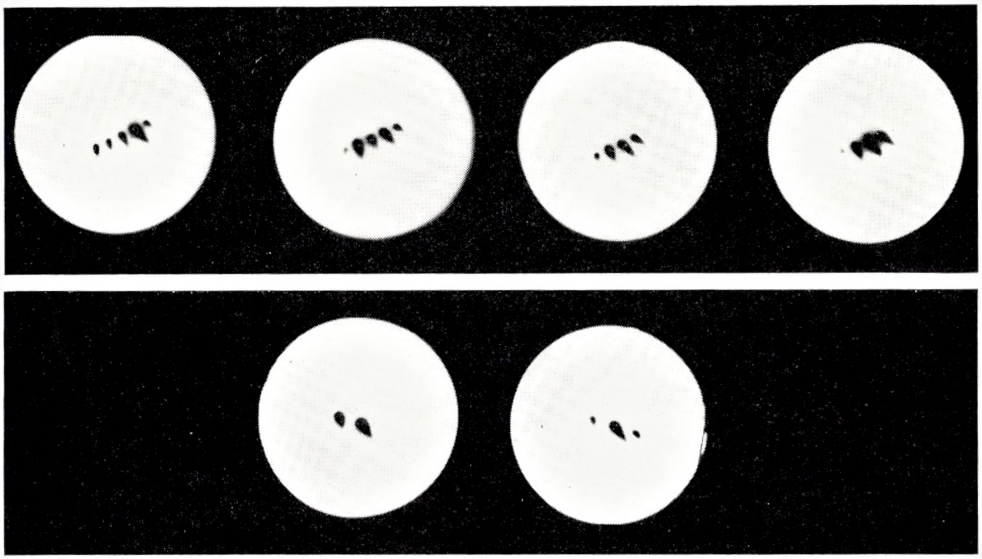

Fig. I.5: Film exposures of the forward beam for the 0.2–0.3 μm sample. The upper series of four exposures corresponds to the incidence angles of $3\theta_B$, $2\theta_B$, and θ_B, and 0 with respect to a {111} plane. The lower two exposures correspond to incidence angles of θ_B and 0 with respect to a {110} plane.

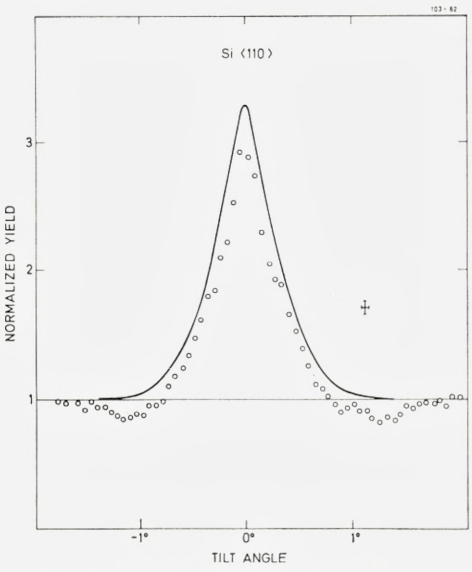

Fig. I.6: Scan through the ⟨110⟩ axis for the 0.2–0.3-μm sample. The experimental results are compared to the classical formula derived in the Appendix. The calculated excess yield has been multiplied by 0.5 to account approximately for inelastic scattering. The error flag on the upper right-hand side indicates beam divergence and statistical uncertainty of the measurements.

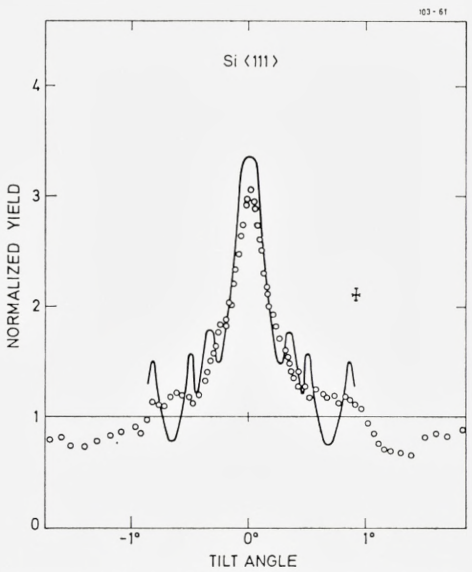

Fig. I.7: Scan through a ⟨111⟩ axis for the 0.2–0.3-μm sample. The experimental results are compared to the peak in yield obtained from a 49-beam calculation. Effects of thermal vibrations are included, but inelastic scattering is not. Instead, the calculated increase in yield has been multiplied by 0.5 as in the previous figure (cf. also Fig. II.4).

{110} and {100} planes are regularly spaced. Finally, we note that the beam collimation was not sufficient to resolve the "wiggles" at high-order Bragg-reflection positions. There are, however, slight indications of these wiggles, especially in the {100} scan.

For selected directions of indicence, photographic exposures of the transmitted beam were taken. Two series of exposures are shown in Fig. I.5. The upper four exposures correspond to beam incidence at angles $3\theta_B$, $2\theta_B$, θ_B, and 0 (left to right) relative to a {111} plane. In this case, the Bragg angle is $\theta_B \simeq 0.1°$, and the distance between the spots is $2\theta_B \simeq 0.2°$. The spot corresponding to the incidence direction is the most intense one (second from the right). Below are two exposures for beam incidence at an angle of $\theta_B \simeq 0.17°$ and parallel to a {110} plane, respectively. All spots in the figure

have a pronounced tail. This corresponds to a low-energy tail of the beam-energy distribution since electrons of lower energies are deflected slightly more by the earth magnetic field.

Scans through the ⟨110⟩ and ⟨111⟩ axes are shown in Figs. I.6 and I.7. The peaks are much stronger than the planar ones, rising by about a factor of three over normal yield. The ⟨110⟩ peak is compared to the classical prediction derived in the Appendix. The theoretical curve is multiplied by a factor of 0.5. The width and shape of the peak are then quite well reproduced. Since the attenuation with depth is expected to be stronger than for planes, also the absolute agreement is reasonable.

The peak along the weaker ⟨111⟩ axis is compared to a many-beam calculation, multiplied also by a factor of 0.5, to correct roughly for inelastic scattering (cf. Sec. II.7). The widths are in good agreement and significantly narrower than predicted by a classical estimate. This qualitative difference between the two axes is also apparent in the diffraction patterns discussed below.

Film exposures of the transmitted beam for incidence close to an axis are shown in Fig. I.8. The exposures in the upper series are taken at tilts of 0.6°, 0.4°, 0.2°, and 0° from the ⟨111⟩ direction. The series below corresponds to incidence angles of 0.75°, 0.50°, 0.25°, and 0° relative to a ⟨110⟩ direction (from left to right). The strongest spot, corresponding to the incidence direction, is fairly easy to identify in the upper series. In the lower series, the spots are very poorly resolved, but it is evident that quite a large number of reflections are excited. Especially at the larger tilt angles to the ⟨110⟩ axis, the scattering is clearly seen to be confined to a ring around the axis, corresponding to conservation of transverse energy[5]. In the terminology of the theory of electron diffraction, the observed pattern is denoted the zero-order Laue zone and corresponds to the intersection of the Ewald sphere with a plane in the reciprocal lattice[14].

2.8-μm *crystal.* Angular scans through the three major planes, {111}, {110}, and {100}, are shown in Figs. I.9–I.11. The peaks are much smaller than those for the thinner crystal, indicating a strong depth dependence. Once again, we may estimate the thickness corresponding to a reduction by $1/e$, assuming exponential attenuation. In this case it turns out to be $\sim 0.4\ \mu$m, in reasonable agreement with the estimate based on the thin-crystal result. The assumption of exponential damping is obviously very crude. The peak shapes are now quite different. The dips are relatively more pronounced, and the widths are narrower, especially for the {111} plane. (cf. the discussion in Sec. II.7).

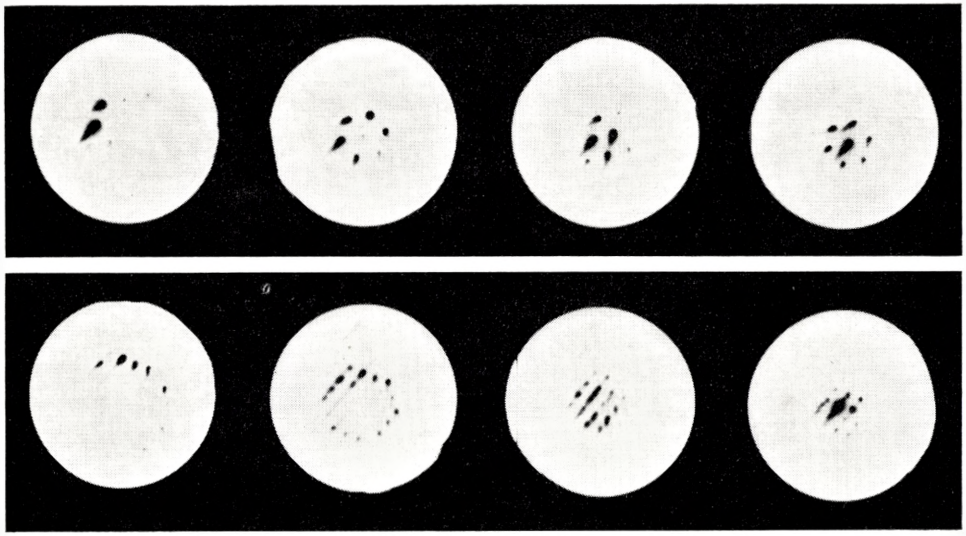

Fig. I.8: Film exposures of the forward beam for the 0.2–0.3 μm sample. The upper series corresponds to incidence angles of 0.6°, 0.4°, 0.2°, and 0°, relative to a $\langle 111 \rangle$ axis, the lower series to incidence angles of 0.75°, 0.50°, 0,25°, and 0°, relative to a $\langle 110 \rangle$ axis.

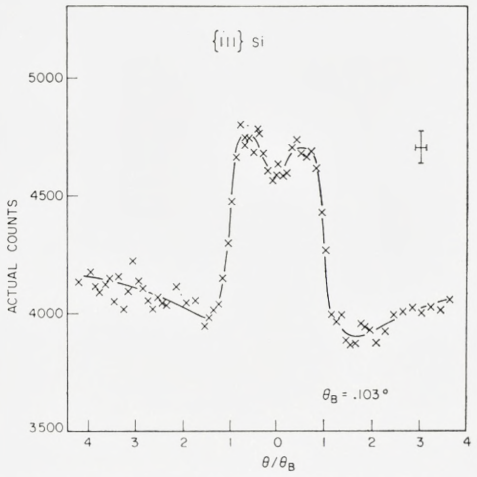

Fig. I.9: Scan through {111} plane for the 2.8-μm sample. The error flag on the upper right-hand side indicates beam divergence and statistical uncertainty of the measurements.

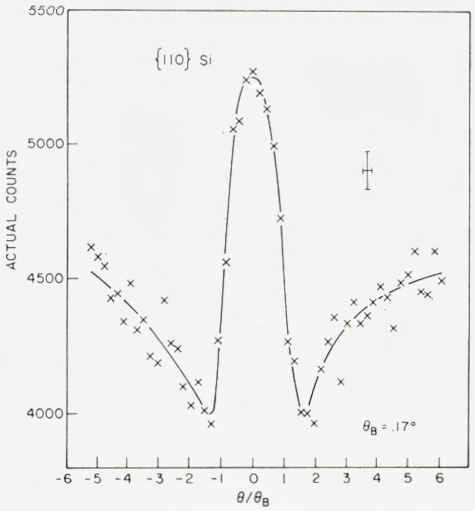

Fig. I.10: Scan through {110} plane for the 2.8-μm sample. The error flag on the upper right-hand side indicates beam divergence and statistical uncertainty of the measurements.

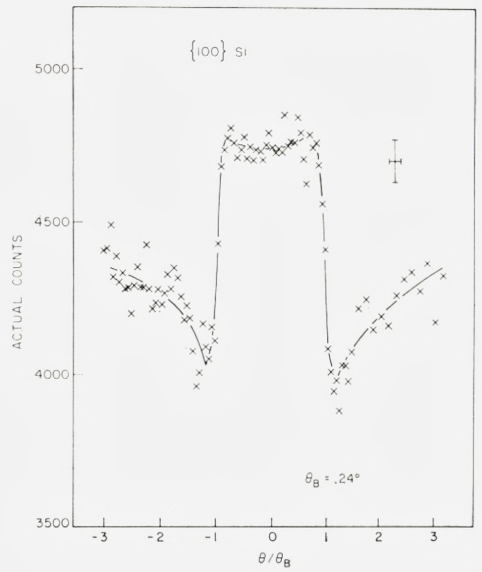

Fig. I.11: Scan through {100} plane for the 2.8-μm sample. The error flag on the upper right-hand side indicates beam divergence and statistical uncertainty of the measurements.

Scans through the ⟨111⟩ and ⟨110⟩ axes are shown in Figs. I.12 and I.13. The peak heights are strongly reduced, and a lot of fine structure has developed. An angular width is difficult to define, but it is obvious that the peaks are much broader than for the thinner crystal. No attempt has been made to check the suggested conservation of the peak volume[11,12]. To calculate this, it would have been necessary to assume azimuthal symmetry of the peak which, for the present measurements, would have been altogether too bold. The decrease in peak height is certainly to some extent counteracted by a broadening of the peak. This is qualitatively different from the planar case, which can be related to the fact that at least from classical estimates, the compensation of the peak for planes is concentrated in a narrow, negative shoulder, whereas for an axis the compensation is shallow and stretches out to angles of order $2a/d$. In the present cases, $2a/d \simeq 4°$.

Film exposures of the transmitted beam are shown in Fig. I.14 for incidence parallel to the two axes ⟨111⟩ and ⟨110⟩ and the three planes {100}, {110}, and {111}. The quality of the pictures is very poor compared to the beautiful Kikuchi patterns obtainable in electron microscopy, where a wealth of lines are resolved[33]. It does, however, suffice to demonstrate two qualitative features: (i) In contrast to Fig. I.5, the angular distribution of the electrons after their passage through a 2.8-μm crystal is determined by multiple (inelastic) scattering. (ii) In analogy to the star patterns observed for

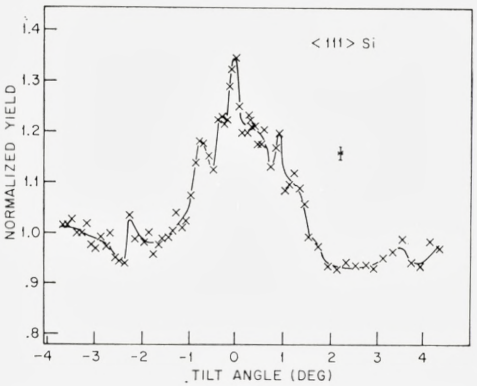

Fig. I.12: Scan through ⟨111⟩ axis for the 2.8-μm sample. The error flag on the upper right-hand side indicates beam divergence and statistical uncertainty of the measurements.

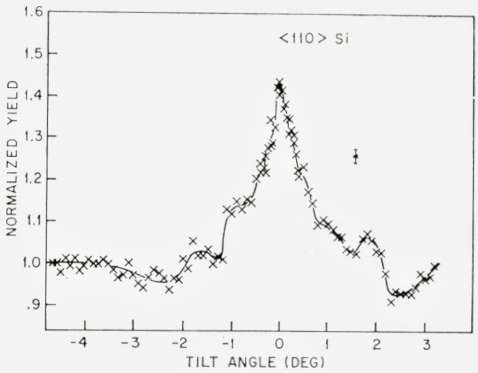

Fig. I.13: Scan through ⟨110⟩ axis for the 2.8-μm sample. The error flag on the upper right-hand side indicates beam divergence and statistical uncertainty of the measurements.

protons transmitted through thin single crystals[27], there are minima in the intensity at angles associated with a high large-angle scattering yield and, conversely, there are maxima at angles associated with a low yield.

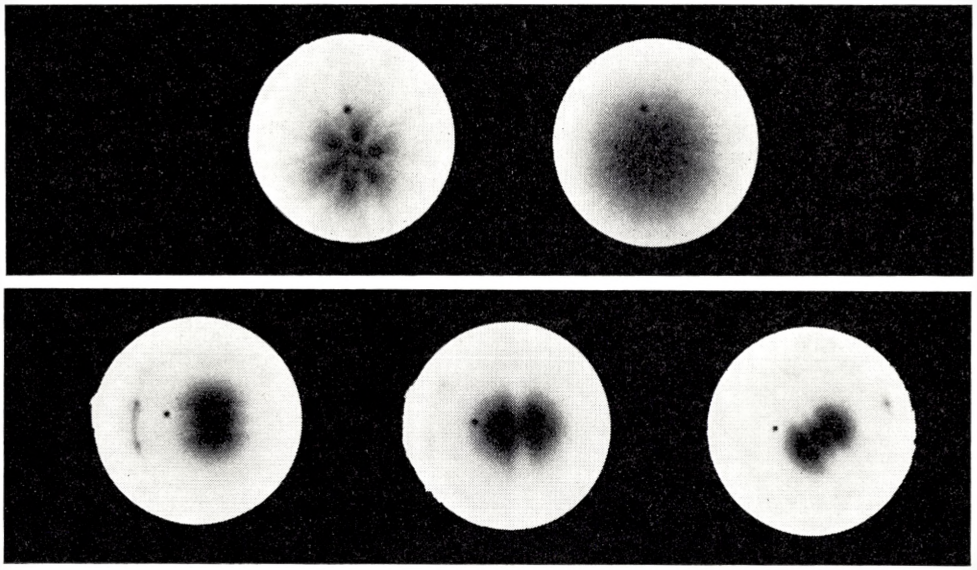

Fig. I.14: Film exposures of the beam transmitted through the 2.8 μm crystal. The upper two exposures correspond to beam incidence parallel to a ⟨111⟩ axis and a ⟨110⟩ axis. The lower three exposures correspond to incidence along {100}, {110}, and {111} planes. The small intense spot visible in all exposure is due to x rays produced in the gold scattering foil.

II. Wave-Mechanical Description

The calculations leading to the theoretical curves in some of the preceding figures (I.2–I.4 and I.7) are based upon the dynamical theory of electron diffraction[14]. Similar calculation have been published by several authors[13, 18–21]. A brief description was also given in connection with the measurements on positron channeling[8, 9]. The following presentation is intended to serve as a basis for the discussion of correspondence in the following chapter and therefore emphasizes the analogy with the classical description of directional effects[5] and uses the notation belonging to that description. This is in accordance with the quantal treatment by LERVIG et al.[10], and we shall at first follow their development and discuss the derivation of the two-dimensional wave equation from the three-dimensional Klein-Gordon equation. In this context, the 'many-beam' formulation of the dynamical theory of electron diffraction then appears as an approximation procedure for solving by Fourier expansion the equation of motion in the continuum approximation.

II.1. Basic wave equation

First, we derive the basic wave equation for the transverse motion, following the procedure of LERVIG et al. Suppose the interaction between particle and lattice can be described by a potential,

$$V(\bar{R}) = V(z, \bar{r}) = \sum_i V_a(\bar{R} - \bar{R}_i), \tag{II.1}$$

where $\bar{R} = (x, y, z)$ is the position of the particle and $\bar{r} = (x, y)$, while the $\bar{R}_i$'s are atomic positions and V_a the atomic potential. The z axis is parallel to an axis or plane, and the particle is assumed to move nearly parallel to it. Since we are concerned with particles at relativistic velocities, we base the discussion on the Klein-Gordon equation for a particle of total energy E and rest mass M_0,

$$\{(\hbar c)^2 \Delta_{\bar{R}} + [(E - V(z,\bar{r}))^2 - M_0^2 c^4]\}\psi(\bar{R}) = 0. \tag{II.2}$$

By describing the interaction with the crystal by a potential (Eq. (II.1)) and disregarding the degrees of freedom belonging to atoms, we have at first neglected inelastic scattering by electrons and phonons, which leads to incoherence of the particle wave function. Furthermore, when the description is based upon the Klein-Gordon equation rather than the Dirac equation, spin-dependent terms in the Hamiltonian are neglected.

The incident particle may be represented by a plane wave,

$$\psi_0(\bar{R}) = e^{i\bar{k}\cdot\bar{R}}, \quad E^2 = (\hbar c)^2 k^2 + M_0^2 c^4. \tag{II.3}$$

Since the scattering at high particle energies is strongly forward-peaked, the interaction with the lattice only leads to transfer of rather small momenta in the x and y directions, the momentum in the z dirsction being approximately conserved. The motion may therefore be separated into a transverse motion in the x–y plane and a longitudinal motion in the z direction with constant velocity $v_z \simeq v = \hbar k/M$, where M is the relativistic mass, $M = E/c^2$. For the transverse motion it is then natural to introduce time, $t = z/v$, as a parameter. The wave function is written as

$$\psi(\bar{R}) = e^{ikz} \cdot u(z,\bar{r}). \tag{II.4}$$

When this is inserted into Eq. (II.2) and we neglect a term V^2 compared to $2EV$ and $\partial^2/\partial z^2$ compared to $2k\partial/\partial z$, corresponding to scattering by small angles only, an equation of a type of a time-dependent, non-relativistic Schrödinger equation for the transverse motion is obtained,

$$\left.\begin{aligned} i\hbar \frac{\partial}{\partial t} u(t,\bar{r}) &= Hu(t,\bar{r}) \\ H &= -\frac{\hbar^2}{2M}\Delta_{\bar{r}} + V(t,\bar{r}). \end{aligned}\right\} \tag{II.5}$$

For a discussion of the corrections to the approximations leading to Eq. (II.5), the reader is referred to Lervig et al.[10].

II.2. Continuum approximation

Let the crystal surface correspond to $z = vt = 0$. For $t < 0$, the potential is zero, and according to Eqs. (II.3) and (II.4), the transverse wave function is then

$$\left.\begin{aligned} u(t,\bar{r}) &= \exp\{i\bar{k}\cdot\bar{R} - ikz\} \simeq \exp\{i\bar{k}_\perp\cdot\bar{r} - iE_\perp t/\hbar\} \\ E_\perp &= \frac{\hbar^2 k_\perp^2}{2M} \simeq E - [(\hbar c)^2 k_z^2 + M_0^2 c^4]^{1/2} \\ \bar{k} &= (\bar{k}_\perp, k_z) = (k_x, k_y, k_z). \end{aligned}\right\} \quad \text{(II.6)}$$

At time $t = 0$, the potential changes suddenly. In the axial case, it is for $t > 0$ a periodic function of t, with period $\tau = d/v$, where d is the spacing of atoms in the strings. In the continuum approximation, this time-dependent potential is replaced by its time average,

$$V(\bar{r}) = \frac{1}{\tau}\int_t^{t+\tau} V(t,\bar{r})\,dt, \quad t > 0. \qquad \text{(II.7A)}$$

The question of the validity of this approximation was studied in detail by LERVIG et al. Also in the classical treatment of directional effects, this question is crucial. For the axial case, the accuracy of the continuum description may be assessed by the more accurate halfway-plane treatment[5, 10]. It turns out that the continuum picture is obtained in the limit of high particle velocities where the time interval τ between collisions becomes short.

In the planar case, the continuum approximation is obtained by averaging the potential along both the z axis ('time average') and the transverse coordinate y parallel to the plane,

$$V(x) = \frac{1}{A}\int_A dy\,d(vt)\,V(t,\bar{r}). \qquad \text{(II.7B)}$$

The accuracy of this approximation has not been studied by a systematic approximation procedure like the halfway-plane treatment of the axial case. In the classical description[5], the continuum approximation was seen to break down at distances from a plane of order a, the Thomas-Fermi screening distance, even for very large particle velocities.

In the dynamical theory of electron diffraction, the continuum approximation corresponds to a Fourier expansion of the lattice potential in one or two dimensions, for the planar and axial case, respectively. It is argued[14] that for high-energy electrons incident at a small angle to a plane (or an axis), only reciprocal lattice points on a line (or a plane) perpendicular to the plane (or axis) are close enough to the Ewald sphere for the corresponding reflections to be appreciably excited. The important question remains, whether scattering processes leading to nonconservation of transverse energy

are weak enough to be treated as a perturbation. Such processes may be either inelastic scattering, or elastic scattering corresponding to reciprocal lattice points off the line (or plane) perpendicular to the plane (or axis). For the axial case, the importance of the latter type was assessed in Ref. 10.

We shall base our discussion of correspondence in the following chapter on the continuum picture, mainly because this leads to rather simple results in both classical and quantal treatments. In so far as the main difference between the results consists of fine structure due to wave interference, the difference may be reduced by inelastic scattering leading to incoherence of the wavefunction.

II.3. Solution of wave equation

In order to solve Eq. (II.5) for $t > 0$, we consider the stationary wave equation corresponding to well-defined transverse energy $E_\perp$. For simplicity, we restrict ourselves to the planar case,

$$\left.\begin{aligned} \left[-\frac{\hbar^2}{2M}\frac{\partial^2}{\partial x^2} + V(x)\right] u^j(x) &= E_\perp^j u^j(x), \\ u^j(t,x) &= u^j(x)\, e^{-iE_\perp^j t/\hbar}, \end{aligned}\right\} \quad \text{(II.8)}$$

where $u^j(x)$ is the eigenfunction belonging to the eigenvalue $E_\perp^j$. The Hamiltonian is invariant under transformations $x \to x + nd_p$, where n is an integer and, consequently, $u^j(x)$ can be written as a Bloch wave,

$$u^j(x) = e^{ik_\perp x}\omega^j(x), \quad \text{(II.9)}$$

where $\omega^j(x)$ is a periodic function, $\omega^j(x + nd_p) = \omega^j(x)$. In order to find solutions (II.9) to (II.8), we expand the potential as well as the wave function in a Fourier series,

$$V(x) = \sum_n V_n e^{ingx} \quad \text{(II.10)}$$

$$\omega^j(x) = \sum_m C_m^j e^{imgx} \quad \text{(II.11)}$$

where g is the length of the reciprocal lattice vector corresponding to the distance d_p between neighbouring planes, $g = 2\pi/d_p$.

If we insert (II.10) and (II.11) in (II.8), and identify terms with the same exponential factor, we obtain for the coefficients C_n^j

$$\frac{\hbar^2}{2M}(k_\perp + ng)^2 C_n^j + \sum_m C_m^j V_{n-m} = E_\perp^j C_n^j. \quad \text{(II.12)}$$

This system of equations leads to approximate eigenfunctions when only a finite number of terms in (II.10) and (II.11) are included. In the terminology of diffraction therory, the term in (II.11) with $n = 0$ is the primary beam, whereas terms with $n \neq 0$ correspond to diffracted beams. A calculation including N terms in the expansions (II.10) and (II.11) is therefore denoted an N-beam calculation. The system of equations (II.12) then reduces to an eigenvalue problem for an $N \times N$ matrix $\tilde{A}$ given by

$$\left.\begin{aligned} A_{nm} &= V_{n-m}, \quad n \neq m \\ A_{nn} &= \frac{\hbar^2}{2M}(k_\perp + ng)^2 + V_0. \end{aligned}\right\} \quad \text{(II.13)}$$

In an N-beam calculation there are for fixed $k_\perp$ N eigenvalues $E_\perp^j$ corresponding to N orthogonal wave functions $u^j(x)$ given by (II.9) and (II.11). The dependence of the exact eigenvalues and eigenfunctions on $k_\perp$ is periodic with period g. For the solutions of a truncated matrix (II.13), this periodicity will only hold approximately within a limited range of $k_\perp$ values. In practice, the number of beams is chosen to be large enough for this range to comprise the interesting range of incidence angles.

II.4. Scattering yield

At first we estimate the atomic scattering yield relative to the random case, corresponding to an eigenfunction $u^j(x)$. For large-angle scattering, the contributions from different atoms are incoherent due to the recoil. Classically large-angle scattering of energetic particles corresponds to collisions with very small impact parameter, and the yield will therefore be proportional to the particle flux at atomic positions. The classical picture applies when the quantity $\varkappa$, defined in Eq. (I.2), is large compared to unity. In the opposite limit of small $\varkappa$ values, the scattering by a single atom may be calculated in the Born approximation. The yield is then proportional to the square of the matrix element $\langle u^l | V_a | u^j \rangle$, where u^j and u^l are the initial and final states of the projectile and V_a is the atomic potential. For large-angle-scattering corresponding to a transfer of a large transverse momentum $\hbar \Delta k$, the matrix element receives its major contribution from distances $\leqslant 1/\Delta k$ from the the center of the atom. If the initial wave function does not vary significantly over distances $\sim 1/\Delta k$, the yield will then also in this limit be proportional to the intensity $|u^j|^2$ at the position of the atom. This result is therefore obtained as a direct consequence of our basic assumption of predominance of

small-angle scattering, which implies that in the matrix (Eq. (II.13)), only Fourier components corresponding to $ng \ll \Delta k$ need be included.

If the intensity distribution $|u^j(x)|^2$ varies only little over a distance $\sim \varrho$, the R.M.S. vibrational amplitude perpendicular to the plane, the yield π_j is given approximately by the intensity at the equilibrium position,

$$\pi_j = |u^j(0)|^2 = (\sum_n C_n^j)^2. \tag{II.14}$$

Here, and in the following, we assume the coefficients C_n^j to be real, which may always be achieved if the crystal has reflection symmetry. Also, for simplicity, we have assumed that $x = 0$ corresponds to the position of the atomic plane. The two assumptions are not always compatible as, e.g., they are not for a {111} plane in a diamond lattice (cf. Fig. I.2 and the corresponding comment in the text). In such cases, the appropriate phase factor must be included in Eq. (II.14), which is modified to

$$\pi_j = \sum_{n,m} C_n^j C_m^j e^{i(n-m)gx_0}, \tag{II.14a}$$

when the atomic plane is at $x = x_0$.

As in the classical description[29], the most important correction for thermal vibrations is the modification of the yield π_j due to displacements of the scattering centers from the plane. When the intensity is averaged over a Gaussian distribution of displacements, Eq. (II.14) is modified into

$$\pi_j = \sum_{m,n} C_n^j C_m^j D_{nm}, \tag{II.15}$$

where D_{nm} are factors of Debye-Waller type,

$$D_{nm} = \exp\{-\tfrac{1}{2}(n-m)^2 g^2 \varrho^2\}. \tag{II.16}$$

A less significant effect of thermal vibrations is the modification of the lattice potential. Incoherence due to atomic recoil reduces the coherent scattering, and this may be taken into account by multiplying the Fourier components of the potential by a Debye-Waller factor,

$$V_n \to V_n D_{no}, \tag{II.17}$$

where D_{no} is given by Eq. (II.16). The corresponding reduction of large Fourier components may alternatively be interpreted as being due to the smearing of the planar potential which results from a convolution with the Gaussian probability distribution for the position of atoms relative to the plane.

The corrections (II.15) and (II.17) only become important when the wave function contains Fourier components corresponding to transverse wave vectors $ng \gtrsim 1/\varrho$. Since $d_p/\varrho \gtrsim 30$ this will only be the case when at least 5–10 beams have to be included in the calculation.

II.5. Surface transmission

The wave function for $t > 0$ may be expanded in terms of eigenfunctions,

$$u(t,x) = \sum_j \alpha_j u^j(x) e^{-iE_\perp^j t/\hbar} = e^{ik_\perp x} \sum_j \alpha_j e^{-iE_\perp^j t/\hbar} \sum_n C_n^j e^{ingx}, \qquad \text{(II.18)}$$

where we have utilized that matching at the surface ($t = 0$) to the incoming plane wave requires all eigenfunctions in Eq. (II.18) to correspond to the value of $k_\perp$ determined by Eq. (II.6). Also the coefficients α_j are determined by this matching, and we obtain

$$\sum_j \alpha_j C_n^j = \delta_{no}. \qquad \text{(II.19)}$$

If the eigenfunctions are normalized,

$$\sum_n C_n^j C_n^k = \delta_{jk}, \qquad \text{(II.20)}$$

it is easily seen that

$$\alpha_j = C_o^j. \qquad \text{(II.21)}$$

Neglecting at first thermal vibrations, we then obtain for the yield P of large-angle scattering, combining (II.14) with (II.21),

$$P = \sum_j (C_o^j)^2 \pi_j = \sum_j (C_o^j \sum_n C_n^j)^2. \qquad \text{(II.22)}$$

If thermal vibrations are taken into account, Eq. (II.14) is replaced by (II.15), and we obtain

$$P = \sum_j (C_o^j)^2 \sum_{m,n} C_n^j C_m^j D_{nm}. \qquad \text{(II.23)}$$

In Eqs. (II.22) and (II.23) we have added the contribution from different eigenfunctions incoherently. The results therefore apply to measurements which are averages over a thickness large enough to correspond to large variations of the relative phase of different eigenfunctions. This assumption of random relative phases is analogous to the assumption of statistical equilibrium in the classical treatment.

The yield of large-angle scattering is determined by the spatial intensity distribution of the channeled particles. By a transmission measurement of the intensity of different Bragg spots, one may determine the distribution in momentum space[34]. The corresponding formulae may easily be derived, but we shall instead turn to the problem of incoherent scattering which, in the theory of electron diffraction, plays a role very similar to that of dechanneling by multiple scattering in the classical theory of channeling.

II.6. Incoherent scattering

An order-of-magnitude estimate of the total cross section for scattering by atoms in a random medium was given in the previous chapter (Eq. (I.1)). For a wave function with high intensity at the atomic sites, there will be a strong increase in scattering. On the other hand, for small scattering angles, the intensity is mainly concentrated in the coherent Bragg peaks. A cursory estimate of the corresponding reduction of in coherent scattering may be obtained from the scattering law applied in the previous estimates,

$$d\sigma(\theta) \propto \frac{d(\theta^2)}{(\theta^2 + \theta_0^2)}. \tag{II.24}$$

Here, θ_0 is given by the ratio of the electron wavelength $\lambda\!\!\!^{-}$ to the screening radius a, $\theta_0 = \lambda\!\!\!^{-}/a$. Since the incoherent scattering is proportional to a factor $[1 - \exp(-\varrho^2\theta^2/\lambda\!\!\!^{-2})]$, a rough estimate of the incoherent fraction is

$$\frac{\sigma_{\text{inc}}}{\sigma_{\text{tot}}} \simeq \frac{1}{\sigma_{\text{tot}}} \int d\sigma(\theta)\Big|_{\varrho^2\theta^2/\lambda\!\!\!^{-2} > 1} = [1 + a^2/\varrho^2]^{-1}. \tag{II.25}$$

In silicon this estimate leads to a rather small incoherent fraction, $\simeq 1/6$. In view of the rough approximations made in the calculation, this number should be considered only as an indication of the importance of corrections for coherent scattering to the inelastic scattering cross section. If the atomic scattering is strongly reduced, inelastic scattering by electrons may play a significant role especially for low Z_2. It should be noted, however, that the enhancement of incoherent scattering (anomalous absorption) corresponding to the increase in large angle scattering yield will be much stronger for thermal scattering than for electronic scattering.

A considerable amount of work has been devoted to the problem of estimating inelastic scattering in connection with electron microscopy. Recently, a review was given by Howie and Stern[35], which also may be

consulted for further references. Usually, inelastic scattering is taken into account by adding an imaginary part to the potential. Such a simple treatment will probably not suffice in the present connection. Since the inelastically scattered electrons also contribute to the large-angle scattering yield, we are concerned not only with the effect of inelastic scattering on the initial, coherent wave function – absorption – but also with the properties of the final states. Thus it may be complicated to introduce inelastic scattering even in the comparatively simple two-beam case[17]. As a first approximation, the final states may be assumed to be plane waves[36]. For the thermal scattering, which involves rather large momentum transfers, this assumption may not be too bad. Since, however, for scattering by electrons, the cross section is strongly peaked at small momentum transfers, the wavefunction may not change its symmetry even after several plasmon excitations[14, 35].

In the axial case, the problem of incoherent scattering is particularly severe. The strong potential minimum should lead to fairly localized states and a large peak in scattering yield. Such states will be highly unstable, and the incoherent scattering cannot be treated as a small perturbation. A treatment in terms of statistical concepts may then be more appropriate[11, 37].

II.7. Numerical evaluation and comparison to experiment

When only a small number of Fourier components (beams) are included, the many-beam formalism lends itself readily to numerical evaluation. Planar peaks in scattering yield for 700-keV electrons along {111} and {110} planes in silicon are shown in Figs. II.1 and II.2. A fairly rapid convergence with increasing number of beams is indicated. The number of beams necessary in such a calculation depends on the strength of the planar potential and the relativistic particle mass. In the present case, 7–9 beams are sufficient for the most closely packed plane, the {111} plane, whereas for the weaker {110} and {100} planes, only 5–7 and 3–5 beams, respectively, are needed.

The relative excitation of different Bragg-reflected beams can be directly observed in the photographic exposures of the transmitted beam (Fig. I.5). For the {111} plane, both second – and third-order reflections are quite important, and of the order of five beams are strongly excited. It may be noted that due to the already mentioned split of the {111} plane in a diamond-type lattice, the second-order Fourier component of the {111} planar potential vanishes. Thus the second-order beam can only be excited indirectly, and the very strong excitation indicated in Fig. I.5 shows the importance of

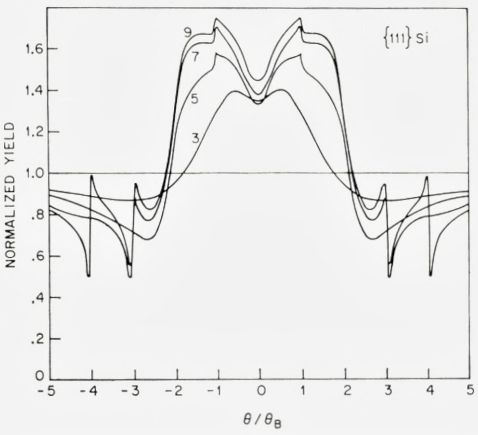

Fig. II.1: Many-beam calculations of the {111} peak for 0.7-MeV e⁻ on Si, including 3, 5, 7, and 9 beams, respectively (static lattice).

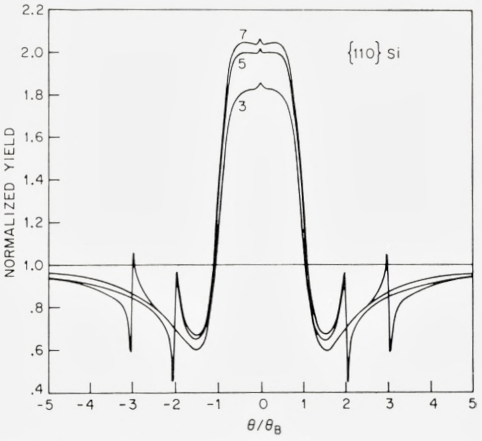

Fig. II.2: Many-beam calculations of the {110} peak for 0.7-MeV e⁻ on Si, including 3, 5, and 7 beams, respectively (static lattice).

dynamical effects. The two exposures for the {110} plane indicate that for this somewhat weaker plane, fewer beams are excited.

In the axial cases, a much larger number of beams are excited simulataeously, as may be appreciated by looking at the Bragg spot patterns in Fig. I.8. For the ⟨111⟩ axis, the number of spots is still fairly small, and a calculation analogous to those for planar cases was therefore attempted (see Fig. I.7). The convergence with number of beams is illustrated in Fig. II.3. For the ⟨110⟩ axis, the spot pattern in Fig. I.8 contains many, fairly weak,

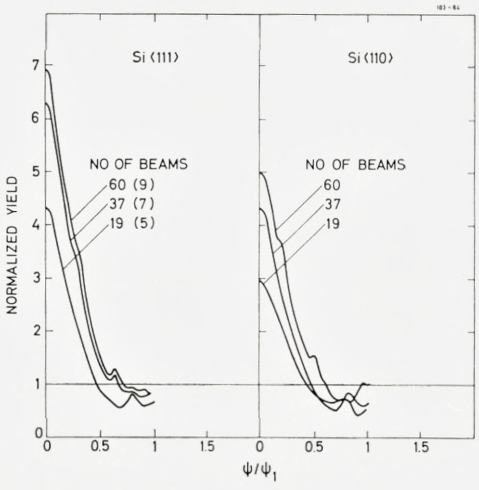

Fig. II.3: Convergence of axial many-beam calculations for 0.7-MeV e⁻ on Si. The number of beams included is indicated in the figure. For the ⟨111⟩ axis, the equivalent number of beams for a {110} planar calculation is given in parentheses. In contrast to the calculations shown in the previous figures, the most important reflections were selected independently for each angle of incidence. Incoherent scattering is neglected, but other effects of thermal vibrations are included (cf. Eqs. (II.15) and II.17)). The values of the characteristic angle ψ_1 for classical channeling are 0.75° and 0.92° for the ⟨111⟩ axis and the ⟨110⟩ axis, respectively.

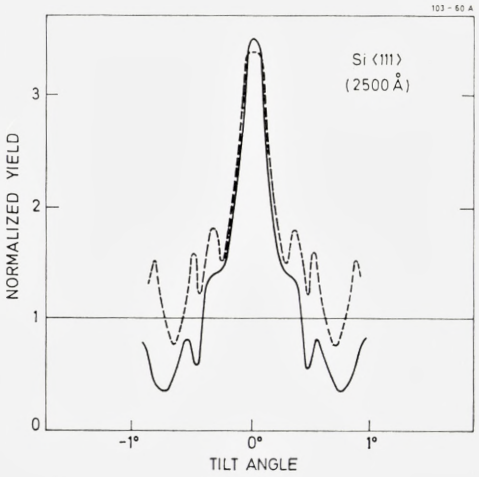

Fig. II.4: Axial peak in large-angle scattering yield for 0.7-MeV e^-, derived from a 49-beam calculation (cf. Fig. II.3). The influence of incoherent scattering has been estimated by including an imaginary component in the potential and assuming scattering into plane-wave states. The magnitude of the imaginary Fourier components of the potential has been evaluated from an approximation to the results given in Ref. 38. The peak derived from this calculation is compared to that obtained without absorption, multiplied by 0.5, corresponding to the correction for inelastic scattering applied in Figs. I.6 and I.7 (dashed curve).

reflections. This may be related to the complicated transverse arrangement of ⟨110⟩ strings and explain the apparent lack of convergence in the many-beam calculations for this case (see Fig. II.3). Also, the ⟨110⟩ axis is somewhat stronger than the ⟨111⟩ axis, and the experimental results were therefore compared (in Fig. I.6) to a classical calculation. It is clear that for a strong, narrow potential, two-dimensional Fourier expansion is basically a very inefficient method.

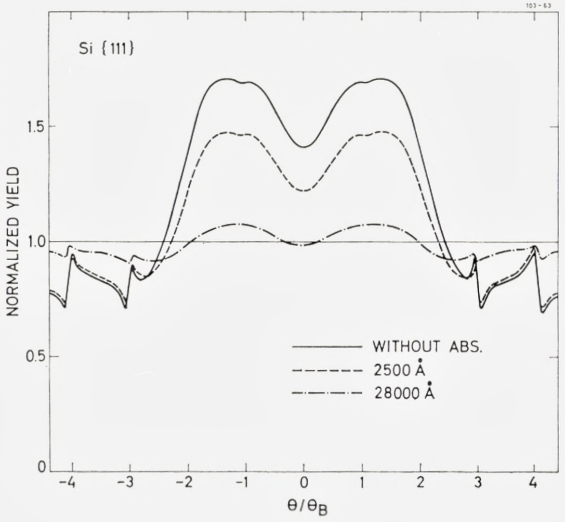

Fig. II.5: 20-beam planar calculation for e^- on Si. Effects of thermal vibration are included according to Eqs. (II.15) and (II.17), and the influence of incoherent scattering has been estimated as described for the previous figure.

As mentioned in the previous section, inelastic scattering is normally in electron microscopy taken into account by adding an imaginary component to the potential, and this treatment may be applied to measurements of large-angle scattering if the final states are assumed to be plane waves. Examples of results from such a procedure are given in Figs. II.4 and II.5 for the $\langle 111 \rangle$ axis and the $\{111\}$ plane, respectively. For the axis, the calculation supports the simple estimate of a reduction by a factor of two, which was applied in Figs. I.6 and I.7. Also for the plane, the result for the thinner crystal is in fair agreement with measurement, but for the thicker crystal, the calculation does not lead to the narrowing of the peak observed experimentally (Fig. I.9). It would seem that measurements of the type described here could serve as a useful tool to test the description of inelastic scattering.

The main conclusion of the comparison between calculations and experiments is, however, that for small depths, the dynamical theory of electron diffraction yields results in good agreement with experiments, at least for planes and weaker axes. A similar conclusion was reached for experiments with positrons[8, 9], and we may therefore in the following investigate the relation to channeling of heavy particles by studying the relationship of this theoretical description with classical channeling theory.

III. Correspondence

III.1. *General considerations*

The main objective of this investigation of electron and positron channeling has been to study the limits for applicability of classical mechanics in the description of channeling phenomena for light particles, and in particular the relation between the theory of electron diffraction, as formulated in Chapter II, and classical channeling theory. In the papers by LINDHARD[5] and LERVIG et al.[10], the validity of classical orbital pictures in the description of collisions with an isolated string was studied in detail with emphasis on the case of heavy particles (protons, α paticles, etc.). For this case it was concluded that in the limit of high particle velocities, a collision with a string of atoms remains classical although classical mechanics does not apply to scattering by a single atom since the quantity $\varkappa$, defined in Eq. (I.2), becomes small compared to unity.

For channeling of light particles (positrons and electrons), an analysis of the interaction with the lattice in terms of scattering of a wave packet by isolated strings or planes may not be appropriate, as the requirements of localization in space and angular spread smaller than a characteristic angle, which for axial channeling is of order[10]

$$\psi_1 = \left(\frac{4Z_1 Z_2 e^2}{pvd}\right)^{1/2}, \tag{III.1}$$

may be mutually exclusive.

Decisive for this question is the magnitude of the number of bound states in the transverse potential minimum. Semiclassically this number may be obtained from the available phase space for transverse energy below the potential barrier. If there are no bound states the scattering is determined by simultaneous interaction with many strings or planes, and no similarity with classical results can be expected. In the limit of many bound states, on the other hand, the classical picture is approached.

In the case of axial channeling, positively charged particles with transverse energy below the barrier for penetration through strings are not bound to one channel but may move freely between strings except at very low transverse energy ('proper channeling'). Still, the number of states per unit cell in the transverse plane (or per string), with transverse energy below the barrier for penetration into strings, is an important quantity. Qualitatively it may be seen from the fact that many states per unit cell are required to form a wave packet which is well localized within this area. More directly, it follows from the quantal treatment in Ch. II. The stationary wave equation (two-dimensional analogue of Eq. (II.8)) may be reduced to one unit cell with periodic boundary conditions, and the conclusions reached in the following concerning the behaviour of the solutions of this equation may therefore be expected also to apply to the axial case for positive particles, with the definition given above for 'the number of bound states'.

At this point it may be appropriate to discuss the special quantal phenomena caused by the lattice periodicity. Indeed the strong diffraction phenomena observed for electrons and positrons constitute the most striking deviation from classical behaviour. The interference due to transverse periodicity with period d_p may be described as a quantization of transverse momentum transfers in bits of $\delta p_\perp = 2\pi\hbar/d_p$, corresponding to an angular deflection of twice the Bragg angle. This quantization was explicitly disregarded by LERVIG et al. on the ground that for particles heavy compared to the electron, $\delta p_\perp$ is very small. In point of fact, for $p_\perp = p\psi_1$, we have[10]

$$\left(\frac{\delta p_\perp}{p_\perp}\right) = \pi\left(\frac{a_0}{d_p}\right)^{1/2}\left(\frac{m_0}{M}\right)^{1/2}(Z_1 Z_2)^{1/2} \ll 1 \quad \text{for} \quad M \gg m_0, \tag{III.2}$$

where M and Z_1 are the mass and charge of the incident particles.

Should we not then, as the essential criterion for classical behaviour, require that the transverse momentum quantum $\delta p_\perp$ be small compared to the transverse momentum corresponding to the potential barier E_b, $p_\perp = (2ME_b)^{1/2}$? Although this is a necessary condition, it is not sufficient. Also the width of the potential minimum is important since, together with the barrier height, it determines the number of bound states.

The interference structure may be smeared by incoherent scattering or poor collimation. This, however, only leads to classical results if the phase-space criterion is fulfilled such that the quantal description leads to a classical envelope with fine structure due to diffraction. In this transition region, deviations from classical results due to tunneling may also be expected.

Channeled positive particles are prevented from penetrating into the center of atoms by the transverse potential barrier. The probability of close encounters with atoms is thereby strongly reduced for incidence parallel to an axis or plane, and the magnitude of this reduction may be sensitive to the probability of tunneling into the classically forbidden regions. Cursory estimates of tunneling probabilities for strings and planes, based upon the WKB approximation, were given in Ref. 10.

We may conclude these general remarks by considering some characteristic lengths, the relative magnitude of which governs the approach towards the classical picture of channeling. The transverse wavelength $\lambda_\perp^b$, which corresponds to a transverse kinetic energy equal to the potential barrier E_b, is given by $2\pi\hbar/(2ME_b)^{1/2}$, where M is the relativistic mass of the particle. This length may first be compared to the width of the potential minimum which, for electrons, is a few times the Thomas-Fermi screening distance a and for positrons is of the order of d, the lattice spacing. When $\lambda_\perp^b$ is small compared to the width, the phase space is large, there will be many bound states, and the quantization of transverse energy may be disregarded.

Second, the importance of the quantization of transverse momentum depends on the relative magnitude of $\lambda_\perp^b$ and the characteristic lengths for lattice periodicity, which again is of order d. If the phase-space criterion is fulfilled, $\lambda_\perp^b$ will be small compared to d, and we may expect interference due to periodicity to lead to fine structure only.

Third, penetration into potential barriers is small if the width of the barrier is large compared to $\lambda_\perp^b$. For positive particles, the barrier widths are of order a or a few times a. Tunneling may therefore lead to important modifications of classical results, even if the phase space is relatively large. In Ref. 8 it was concluded, however, that the influence of tunneling is strongly reduced by the smearing of the distribution of atoms, due to thermal vibrations.

III.2. Analogy between quantal and classical descriptions

In the following we shall try to describe in some detail how the quantal description of channeling approaches the classical description and illustrate the importance of the phase-space criterion. In this connection it is important to specify the type of measurement we are considering. We shall be concerned only with predictions of the dependence on incidence direction of the yield of a close-encounter process such as large-angle scattering or inner-shell excitation. This simplifies the problem considerably since we need not

consider in detail the validity of classical orbital pictures in describing particle trajectories[25] but only the ability of classical mechanics to predict the distribution of particles in the transverse direction or plane. A quantal treatment was discussed in the previous chapter and for the classical description, we may refer to Lindhard's original treatment[5]. Numerical estimates based upon the two formulations are compared in Ch. IV. In the Appendix, an example is given of an analytical calculation based upon the classical description.

The physical situation we are concerned with is an external beam of particles incident on a single crystal at an angle ψ to a major plane (or axis), and we ask for the probability $P(\psi)$ for particles to come close to the center of crystal atoms, as manifested in the yield of a close-encounter reaction. Many similarities are apparent between the classical and the quantal treatments of this problem. Owing to the predominance of forward scattering, the motion of the particles may be separated into a longitudinal motion with nearly constant velocity and a transverse component, which may be described as motion in an averaged potential with approximate conservation of the transverse energy $E_\perp$ ('continuum approximation'). The probability $P(\psi)$ is then determined in two steps:

First, the probability $\pi(E_\perp)$ for a particle with transverse energy $E_\perp$ to have a close encounter with an atom is calculated. In the classical treatment, this involves finding the probability distribution in transverse space as a function of $E_\perp$, based on statistical arguments. In the quantal treatment, $E_\perp$ is quantized. The eigenfunction $u^j(x)$ belonging to an eigenvalue $E_\perp^j$ may be calculated from Eqs. (II.8), (II.9), (II.11), and (II.12). The probability density in transverse space is given by the square of this eigenfunction. In both cases, the reaction yield is assumed to be proportional to the density at atomic positions.

Second, the population of transverse-energy levels is determined by surface transmission. Classically, a particle hitting the crystal at a distance x from a plane acquires a potential energy $V(x)$, leading to a total transverse energy

$$E_\perp = E\psi^2 + V(x). \tag{III.3}$$

Since the intensity of the beam is uniform over the crystal surface, the distribution in transverse energy is then given by

$$W(E)_\perp \propto \int dx \delta(E_\perp - E\psi^2 - V(x)) = \sum_i \left| \frac{\partial V}{\partial x} \right|^{-1}_{x = x_i} \tag{III.4}$$

where the x_i's are solutions to Eq. (III.3). Formulae analogous to (III.3) and (III.4) hold for the axial case.

In the wave-mechanical formulation, the population of energy levels is determined by a matching of the total wave function at the crystal surface to the incident plane wave, which yields the coefficients (Eq. (II.21)) of different eigenfunctions. In the expressions for the total probablility density in the transverse plane, interference between different eigenfunctions is neglected. In the planar case, this corresponds to the assumption of statistical equilibrium in the classical calculation and should be valid for not too small thicknesses. Problems related to the assumption of statistical equilibrium for axial channeling are discussed in Ch. IV and, in more detail, in the Appendix. Deviations from equilibrium close to the surface have been studied extensively for heavy-particle channeling[27] and recently also for electron channeling[37, 39].

In the following we shall analyze both of these steps in detail for the one-dimensional case. In the quantal treatment in Ch. II, the problem of determining eigenfunctions for the transverse Hamiltonian was reduced to solving the Schrödinger equation (II.8) in a finite interval $[0,d_p]$, with periodic boundary conditions according to Eq. (II.9). In order to gain insight into the properties of such solutions, we consider a simpler analogous problem where the particle is confined by infinite potential walls. For the general qualitative conclusions concerning the importance of the magnitude of quantum numbers, the difference in boundary conditions should not be of any importance and, furthermore, the boundary conditions are for strongly bound states determined by the local potential minimum and not by periodicity (cf. also Sec. IV.2).

III.3. Harmonic oscillator

First, we treat the familiar example of a harmonic oscillator. For many physical problems, this is a basic example, which may be solved by analytical methods. In fact, the spatial probability density for a particle bound in a harmonic potential is used as a standard textbook illustration of correspondence with classical mechanics in the limit of large quantum numbers[40]. According to the general discussion above, evaluation of this density is the first task to be performed.

Spatial density. With the potential $V(x) = \frac{1}{2} M\omega^2 x^2$, the eigenvalue equation becomes

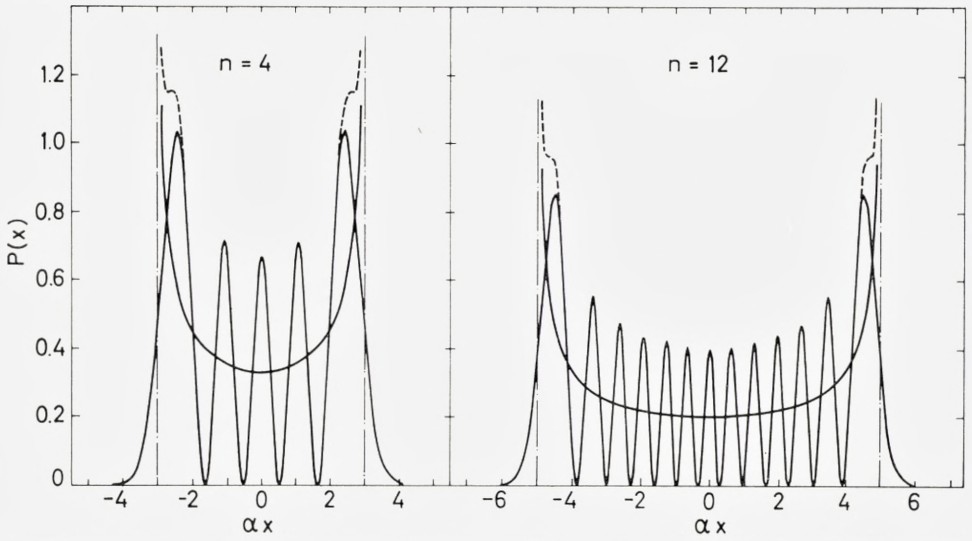

Fig. III.1: Spatial density for harmonic-oscillator eigenfunctions corresponding to n = 4 and n = 12, respectively. The classical turning points are indicated by dot-and-dash lines, and the classical spatial probability (Eq. (III.9)) is given by the smooth solid curve. The oscillating solid curve corresponds to the exact distribution $|u_n(x)|^2$ (Eq. (III.7)) and the dashed curve to the density obtained from the WKB approximation (Eq. (III.22)).

$$\left[-\frac{\hbar^2}{2M}\frac{\partial^2}{\partial x^2}+\tfrac{1}{2}M\omega^2x^2\right]u(x) = Eu(x). \tag{III.5}$$

Here, and in the following, the transverse energy is denoted simply by E. This equation has the well-known solutions

$$E_n = \hbar\omega(n+\tfrac{1}{2}), \tag{III.6}$$

and

$$u_n(x) = N_nH_n(\alpha x)e^{-1/2\,\alpha^2x^2}, \tag{III.7}$$

where $\alpha^2 = M\omega/\hbar$, H_n is the n'th Hermite polynomial, and N_n is a normalization constant,

$$N_n = \sqrt{\alpha}/(\sqrt{\pi}2^n n!)^{1/2}. \tag{III.8}$$

The probability density, $|u(x)|^2$, is in Fig. III.1 compared to the classical distribution,

$$\varrho(x) = \left(\frac{M\omega^2}{2\pi^2}\right)^{1/2}(E-\tfrac{1}{2}M\omega^2x^2)^{-1/2}, \tag{III.9}$$

for two values of n. For moderately high n, the distributions are very similar except for the rapid oscillations of the quantal density.

Surface transmission. Corresponding to the case where particles are incident on a crystal at an angle φ to a major plane, we now ask for the population of the harmonic-oscillator eigenstates for $\psi(x,\ t=0) = e^{ikx}$, where $\hbar k$ denotes the transverse momentum, related to the total momentum p by $\hbar k = p\varphi$. The classical result is

$$W(E) = 2\left(\frac{\partial V}{\partial x}\right)^{-1}\Bigg|_{V=E-\hbar^2k^2/(2M)} = \left(\frac{2}{M\omega^2}\right)^{1/2}\left(E-\frac{\hbar^2k^2}{2M}\right)^{-1/2}. \qquad \text{(III.10)}$$

In order to find the quantal distribution, we have to evaluate the matrix element

$$\langle u_n \,|\, e^{ikx}\rangle = N_n \int_{-\infty}^{\infty} dx H_n(\alpha x)\, e^{-1/2\,\alpha^2x^2} e^{ikx}. \qquad \text{(III.11)}$$

This integral may be evaluated by repeated partial integration when the following represention of the Hermite polynomial is used,

$$H_n(x) = (-1)^n e^{x^2}\frac{\partial^n}{\partial x^n} e^{-x^2}, \qquad \text{(III.12)}$$

and the result is

$$\langle u_n \,|\, e^{ikx}\rangle = \frac{1}{\alpha} N_n \sqrt{2\pi}\,(-i)^n\, e^{-k^2/(2\alpha^2)} H_n(k/\alpha). \qquad \text{(III.13)}$$

Since Eq. (III.11) is essentially the momentum representation of the n'th state, this result, except for a phase factor, also follows directly from the symmetry between x and $\dfrac{\partial}{\partial x}$ in the Hamiltonian.

The population of the n'th energy level is given by the square of this matrix element,

$$P(E_n) = \left(\frac{2\pi\hbar}{M\omega}\right)\cdot N_n^2 \cdot e^{-k^2/\alpha^2} H_n^2(k/\alpha). \qquad \text{(III.14)}$$

When this expression is divided by the spacing of levels, $h\omega$, the relation to the classical energy distribution (III.10) is the same as the relation between the quantal and classical spatial densities except for the fact that the expressions are now compared as functions of E (cf. Fig. III.3).

Since the main purpose of these considerations is to illustrate the correspondence qualitatively, we shall only for a special case prove that the quantal result approaches the classical one in the limit of large quantum numbers. Consider the energy distribution (III.14) for $k = 0$, corresponding

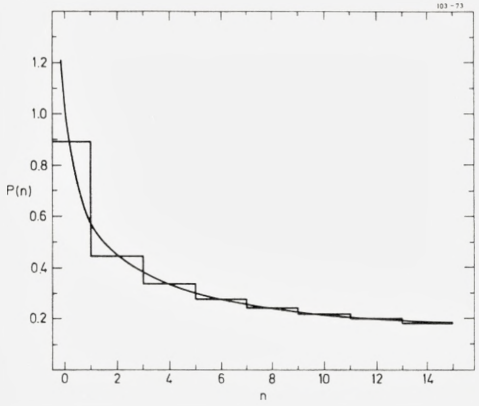

Fig. III.2: Comparison of quantal (Eq. (III.5)) and classical (Eq. (III.10)) energy distributions for $k = 0$, corresponding to incidence parallel to a plane. The two distributions have been multiplied by $1/2(M\omega^2\hbar\omega)^{1/2}$. Here n denotes the level number, i.e., $E_n = (n+1/2)\hbar\omega$, and the staircase distribution gives the population for n even.

for the channeling case to zero angle of incidence with a plane. Only states with even parity are then populated, and we may compare the classical density (Eq. (III.10)) to $P(E_{2n})/(2\hbar\omega)$. Using the relation $H_{2n}(0) = (-1)^n(2n)!/n!$ we obtain

$$P(E_{2n})/(2\hbar\omega) = \left(\frac{2}{M\omega^2}\right)^{1/2} \cdot \frac{1}{(\hbar\omega)^{1/2}} \cdot \left(\frac{\pi}{2}\right)^{1/2} \cdot \frac{(2n)!}{2^{2n}(n!)^2}. \tag{III.15}$$

For large n, we may evaluate the factorials by Stirling's formula,

$$n! \simeq \sqrt{2\pi n} \cdot e^{-n} \cdot n^n \tag{III.16}$$

and obtain

$$P(E_{2n})/(2\hbar\omega) \simeq \left(\frac{2}{M\omega^2}\right)^{1/2} \cdot \frac{1}{(2n\hbar\omega)^{1/2}}. \tag{III.17}$$

This result is essentially identical to Eq. (III.10) for $k = 0$. The distributions (III.10) and (III.15) are compared in Fig. III.2.

III.4. WKB approximation

The general approach to the classical description for large quantum numbers may be seen more directly in the WKB approximation. This semiclassical description offers a convenient stepping stone from a quantal formulation to the classical treatment (cf. also Ref. 25).

Spatial density. A stationary solution to the Schrödinger equation with a potential $V(x)$ may be written

$$\psi(x,t) = C\exp\{i(s(x) - Et)/\hbar\}, \tag{III.18}$$

where the phase function $s(x)$ satisfies

$$\frac{1}{2M}\left(\frac{\partial}{\partial x}s\right)^2 - [E - V(x)] - \frac{i\hbar}{2M}\frac{\partial^2}{\partial x^2}s = 0. \tag{III.19}$$

The WKB approximation obtains the first two terms of a formal expansion of s in powers of $\hbar$. In classically allowed regions, $(E > V(x))$, the general solution in this approximation is[40]

$$\left.\begin{aligned} u_E(x) = Ak(x)^{-1/2}\exp\left\{i\int_{x_0}^{x} k(x')\,dx'\right\} + \\ + Bk(x)^{-1/2}\exp\left\{-i\int_{x_0}^{x} k(x')\,dx'\right\}. \end{aligned}\right\} \tag{III.20}$$

where we have introduced the local wave vector

$$k(x) = \frac{1}{\hbar}(2M(E - V(x)))^{1/2}. \tag{III.21}$$

Apart from oscillations due to interference between the two amplitudes corresponding to opposite directions of the particle velocity, we have $|u(x)|^2 \propto \propto (E - V(x))^{-1/2}$ as for the classical spatial distribution (cf. Eq. (III.9)). The condition for the validity of the WKB approximation is that the fractional change in wavelength be small over a distance of one wavelength. Except for the regions close to the classical turning points ($V(x) \simeq E$), this is in the case of a potential minimum equivalent to a demand for many nodes in the wave function or a large quantum number n.

Surface transmission. Consider for simplicity a symmetric potential $V(x) = V(-x)$ increasing monotonically to infinity for $x \to \infty$ with $V'(x) \neq 0$ for $x \neq 0$. When the solution (Eq. (III.20)) for $V < E$ is matched to the WKB solutions in the classically forbidden regions ($V > E$), the wave function becomes[40]

$$u_E(x) = Ak(x)^{-1/2}\cos\left(\int_{-a}^{x} k(x')\,dx' - \frac{\pi}{4}\right). \tag{III.22}$$

Matching to the solution for $V > E$ at the turning points, $x = \pm a$, leads to quantization of the energy, determined by[40]

$$\int_{-a}^{a} k(x)\,dx = (n + \tfrac{1}{2})\pi, \quad n = 0,1,2, \ldots \tag{III.23}$$

In order to determine the population of eigenstates corresponding to an initial wave function $\psi(x, t = 0) = e^{ik_0 x}$, we consider again the matrix element

$$\langle u_E(x) | e^{ik_0 x} \rangle = A \int k(x)^{-1/2} \cos\left(\int_{-a}^{x} k(x')\, dx' - \frac{\pi}{4} \right) e^{ik_0 x}\, dx. \quad \text{(III.24)}$$

This integral we may evaluate by the stationary-phase method. First, the wave function $u_E(x)$ may be written as a sum of two amplitudes corresponding to opposite directions of the velocity (cf. Eq. (III.20)). A stationary phase, determined by

$$\frac{d}{dx}\left(\pm \int_{-a}^{x} k(x')\, dx' \pm \frac{\pi}{4} + k_0 x \right) = 0, \quad \text{(III.25)}$$

is obtained only for the amplitude corresponding to the velocity direction given by the sign of k_0. For $0 < k_0 < k(0)$, Eq. (III.25) is fulfilled for two values of x, $x = \pm x_k$, determined by

$$k(\pm x_k) = k_0. \quad \text{(III.26)}$$

The contributions from the two x values are then approximately given by the expression

$$\left.\begin{aligned} &\frac{A}{2} k(x_k)^{-1/2} \exp\left\{ -i \int_{-a}^{\pm x_k} k(x)\, dx \pm i k_0 x_k - \frac{i\pi}{4} \right\} \times \\ &\qquad \times \int dx \exp\left\{ i \frac{MV'(\pm x_k)}{2\hbar k_0} x^2 \right\}, \end{aligned}\right\} \quad \text{(III.27)}$$

in which the phase has been expanded to second order around the points $x = \pm x_k$. When the result ($c > 0$)

$$\int_{-\infty}^{\infty} \exp(\pm i c x^2)\, dx = \sqrt{\frac{\pi}{2c}}\,(1 \pm i) \quad \text{(III.28)}$$

is applied, the magnitude of the two contributions may be evaluated, and we obtain

$$P(E) = |\langle u_E(x) | e^{ik_0 x} \rangle|^2 = \frac{2\pi\hbar}{MV'(x_k)} A^2 \cos^2\left(\int_0^{x_k} (k(x) - k_0)\, dx - \frac{\pi}{4} \right), \quad \text{(III.29)}$$

where the argument of the cosine corresponds to half the relative phase of the contributions from $x = \pm x_k$. As for the harmonic oscillator we obtain an energy population which oscillates as a function of energy, and we have

now seen that this behaviour is caused by interference between the amplitudes corresponding to the two points $x = \pm x_k$, at which the velocity of a particle with energy E matches the well-defined velocity for $t = o$, $v = \hbar k_0/M$.

In order to compare with the classical energy population,

$$W(E)dE = 2V'(x_k)^{-1}dE, \tag{III.30}$$

we must evaluate the normalization constant A and furthermore divide $P(E)$ by the splitting ΔE between eigenstates. The normalization is determined by,

$$A^2 \int_{-a}^{a} k(x)^{-1} \cos^2\left(\int_{-a}^{x} k(x')\,dx' - \frac{\pi}{4}\right) dx = 1. \tag{III.31}$$

If the condition for the WKB approximation is fulfilled, the potential varies only little over one wavelength, and we have approximately

$$A^2 \simeq 2\hbar \left\{ \int_{-a}^{a} k(x)^{-1}\,dx \right\}^{-1}. \tag{III.32}$$

The quantization of energy is given by Eq. (III.23). At high quantum numbers, we may evaluate the splitting ΔE from

$$\Delta E \frac{d}{dE}\left(\int_{-a}^{a} k(x)\,dx\right) \simeq \pi. \tag{III.33}$$

With the definition (III.21) of $k(x)$, this leads to

$$\Delta E \simeq \frac{\pi\hbar^2}{M} \left\{ \int_{-a}^{a} k(x)^{-1}\,dx \right\}^{-1}. \tag{III.34}$$

Combining Eqs. (III.32) and (III.34) with Eq. (III.29), we obtain

$$P(E)/\Delta E \simeq (4/V'(x_k)) \cos^2\left(\int_{0}^{x_k} (k(x) - k_0)\,dx - \frac{\pi}{4}\right). \tag{III.35}$$

When averaged over the oscillations, this expression is idential to the classical result in Eq. (III.30).

It should be noted that the method of evaluation used here is limited to energies somewhat larger than classical minimum energy, $E = V(0) + \hbar^2 k^2/(2M)$. Also, for large values of E, the method breaks down because the stationary points $\pm x_k$ are too close to the classical turning points, where the expression (III.22) for the wave function cannot be applied. In these regions, we way instead expand the potential to first order around $x = \pm a$

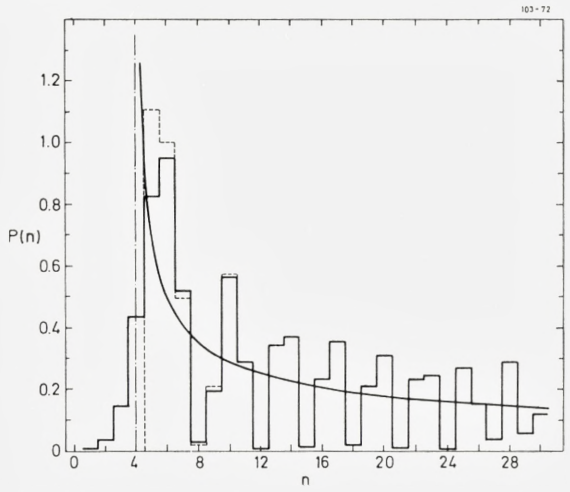

Fig. III.3: Population of levels in harmonic oscillator for $\psi(x, t = 0) = \exp(ikx)$, with a value of k corresponding to $(\hbar k)^2/(2M) = 4.5\ \hbar\omega$. This lower limit for the classical energy population is indicated by a dot-and-dash line, and the classical distribution (Eq.(III.10)) is given by the smooth solid curve. The solid staircase distribution corresponds to the exact population (Eq. (III.14) divided by $\hbar\omega$), while the result obtained from the WKB approximation (Eq. (III.35)) is indicated by the dashed lines. Normalization and notation as for Fig. III.2.

and represent the wave function by an Airy function. For $k = 0$, a result analogous to Eq. (III.35) is then easily obtained, with the cosine replaced by 0 or 1 for odd and even parity, respectively.

We shall not go into the details of such estimates since the main purpose of this chapter is to provide some general insight into the correspondence between classical and quantal results. Such insight is more readily gained from analytical treatments of simple examples than from more realistic numerical calculations, as presented in Ch. IV. For this purpose, the WKB approximation is particularly helpful, yielding basically classical results modulated by oscillations due to interference between different amplitudes.

We conclude this chapter by an assessment of the accuracy of the WKB approximation for the harmonic oscillator, which was treated exactly in the previous section. Figure III.3 shows the population of different energy levels for a plane wave with a k value corresponding to $(\hbar k)^2/2M = 4.5\hbar\omega$. The smooth curve is the classical energy distribution given by Eq. (III.10), while the staircase distributions correspond to the exact quantal result (Eq. (III.14), fully drawn) and the WKB approximation (Eq. (III.35), dashed). Only close to the minimum energy do the two distributions differ enough to be drawn separately. It should be noted that for the harmonic oscillator, Eq. (III.23) reproduces the exact energy quantization. For the spatial density distribution, shown in Fig. III.1, the accuracy of the WKB approximation is similar, and appreciable deviations from the exact results occur only close to the classical turning points. For small values of αx, the distributions deviate by less than one percent.

IV. Applicability of Classical Calculations to Electron and Positron Channeling

In this chapter, we first apply the general quantative results of the previous chapter to obtain approximate criteria for the applicability of classical concepts to channeling of electrons and positrons from estimates of the number of bound states in the transverse continuum potential According to Eq. (III.23), this number may be obtained approximately as the available phase space divided by Planck's constant h (or by h^2 in two dimensions).

Second, the transition to the classical limit at high quantum numbers is studied quantitatively by a comparison of classical results for the directional dependence of the large-angle-scattering yield with results obtained from the many-beam description reviewed in Ch. II. The calculations also provide a check of the formulas for the number of bound states derived from semiclassical estimates.

IV.1. Number of bound states

The following estimates correspond closely to those given in previous work[8–13]. Also in the review by GEMMEL[27], such estimates were given. For the planar case, our results are essentially in agreement, apart from a trivial mistake by a factor of two in his formulas. For axial channeling of negative particles, there is a more important difference in method as well as result.

Planes. The planar potential is illustrated in Fig. IV.1 for positive particles. We base the estimates of the phase space upon Lindhard's standard potential, which for a particle with one positive charge, leads to the planar potential.

$$V(x) = 2\pi Z_2 e^2 N d_p [(x^2 + C^2 a^2)^{1/2} - x], \tag{IV.1}$$

where Nd_p is the density of atoms in the planes, d_p being the planar spacing. The width of the potential maximum is approximately $3Ca$, where a is the Thomas-Fermi screening distance and C a potential parameter, $C \sim \sqrt{3}$.

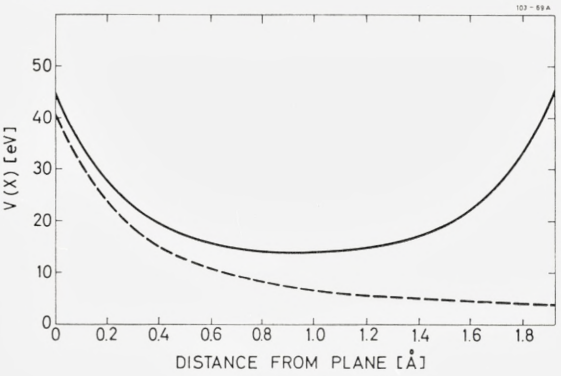

Fig. IV.1: Si {110} planar potential for positrons. The potential from a single plane is represented by the dashed curve (Eq. (IV.1)), while the solid curve is obtained by adding the potential from the neighbouring plane. The phase-space estimates are based on the latter potential.

The number of bound states in the potential is given by

$$\nu_p \simeq \frac{1}{\pi\hbar}\int_0^{d_p}(2M(V_{\max}-V))^{1/2}dx, \tag{IV.2}$$

where M is the relativistic particle mass.

From a numerical integration of (IV.2), we obtain for negative particles a result corresponding approximately to a square-well potential with depth $V(0)$ given by Eq. (IV.1), and width $\sim 3Ca$,

$$\nu_p^- \simeq \left(\frac{M}{m_0}\right)^{1/2}\left(\frac{4a_0}{d_p}\right)[Nd_p^3]^{1/2}, \tag{IV.3}$$

where m_0 is the electron rest mass and a_0 the Bohr radius, $a_0 = 0.53$ Å. For positive particles, the potential minimum is wider by a factor of $\approx d_p/(3Ca)$, and Eq. (IV.2) leads to

$$\nu_p^+ \simeq Z_2^{1/3}\left(\frac{M}{m_0}\right)^{1/2}[Nd_p^3]^{1/2}. \tag{IV.4}$$

The ratio of these two numbers is approximately

$$\nu_p^+/\nu_p^- \simeq Z_2^{1/3}. \tag{IV.5}$$

Even for strong planes, the estimate (IV.3) leads to a number of bound states of the order of unity, $\nu_p^- \sim 1$ for electrons of not too high energy. In contrast, for positrons, the potential minimum between planes may often contain quite a few bound states. We shall return to a more detailed comparison of negative and positive particles below.

Strings. For negative particles, the number of bound states in a string potential is given by

$$\nu_s^- \simeq \frac{1}{4\pi^2\hbar^2}\int d^2\bar{r}\int d^2\bar{p}_\perp\Big|_{E_\perp<0}, \tag{IV.6}$$

where $E_\perp = p_\perp^2/(2M) + U(\bar{r})$, and we have assumed that the continuum potential vanishes far from strings. Performing the integration over transverse momentum, we obtain

$$\nu_s^- \simeq \frac{M}{2\pi\hbar^2}\int d^2\bar{r}\,|U(\bar{r})|. \tag{IV.7}$$

Again we may introduce the standard potential, which for strings leads to

$$U(r) \simeq -\frac{Z_2e^2}{d}\log\left(\left(\frac{Ca}{r}\right)^2+1\right), \tag{IV.8}$$

where d denotes the spacing of the atoms in the string. This corresponds to a rotationally symmetric potential inside the area, $\pi r_0^2 = (Nd)^{-1}$, belonging to one string. Subtracting the value $U(r_0)$ from Eq. (IV.8), we obtain from Eq. (IV.7)

$$\nu_s^- \simeq \frac{M}{2\hbar^2}\cdot\frac{Z_2e^2}{d}(Ca)^2\log\left(\frac{r_0}{Ca}\right)^2. \tag{IV.9}$$

Since normally the log term in (IV.9) is of order 3–4, we obtain[11]

$$\nu_s^- \simeq \left(\frac{4a_0}{d}\right)\cdot\left(\frac{M}{m_0}\right)Z_2^{1/3}. \tag{IV.10}$$

By partial integration, the formula (IV.7) may also be expressed in terms of the average square radius of the atoms,

$$\langle R^2\rangle = Z_2^{-1}\int_0^\infty 4\pi R^4\varrho(R)\,dR, \tag{IV.11}$$

where $\varrho(R)$ is the electron density belonging to one atom. The result is

$$\nu_s^- = \frac{M}{2\hbar^2}\cdot\frac{Z_2e^2}{d}\cdot\tfrac{2}{3}\langle R^2\rangle. \tag{IV.12}$$

For the somewhat more realistic Lenz-Jensen potential, the average-square radius becomes[5] $\langle R^2\rangle \simeq 15a^2$, which again leads to (IV.10). For 1-MeV electrons, this formula gives a number of bound states $\nu_s^- \sim 4$–10 for a major axis.

For positive particles, the accessible area per string is $\sim \pi r_0^2$. If the effective transverse-energy barrier is $\sim \frac{1}{2} pv\psi_1^2$, corresponding to a critical angle[10],

$$\psi_1 = \left(\frac{4Z_2 e^2}{pvd}\right)^{1/2}, \tag{IV.13}$$

we obtain for the number of bound states (or rather states per string with energy below the barrier, cf. sec. III.1).

$$\nu_s^+ \simeq \frac{1}{\pi}\left(\frac{d}{a_0}\right)\left(\frac{M}{m_0}\right) Z_2 (Nd^3)^{-1}. \tag{IV.14}$$

This number is normally quite large, $\nu_s^+ \sim 10^2$ for 1-MeV positrons.

Comparison of different cases. The relationship between the four estimates, Eqs. (IV.3), (IV.4), (IV.10), and (IV.14) is illustrated in Table IV.1 for 1-MeV electrons and positrons along a {110} plane and a ⟨110⟩ axis, respectively, in silicon and gold.

Table IV.1.
Number of bound states for 1-Mev e^+, e^- in Si and Au.

	Silicon		Gold	
	e^+	e^-	e^+	e^-
⟨110⟩	34	4	286	9
{110}	2.5	1.1	9	1.5

These examples clearly indicate the importance of distinguishing between positive and negative particles as well as between axial and planar cases. The difference in magnitude of the number of bound states for axes and planes is, to a large extent, due to the fact that the axial potential is two-dimensional, while the planar potential is one-dimensional. It might therefore be argued that the number of bound states in the planar potential should be compared to the square root of the corresponding number for strings. This, however, would not change the qualitative conclusion drawn from Table IV.1, that classical concepts may be applied more readily to axial than to planar motion. This difference is strongest for high values of Z_2 where also the difference between electrons and positrons is most pronounced.

IV.2. Comparison of classical and quantal calculations

Although the approach towards a classical description is basically governed by the magnitude of quantum numbers, as derived semiclassically above, it must be borne in mind that the validity of classical estimates may depend strongly on the specific phenomenon under observation. In this section, we shall compare directly quantal and classical calculations of the directional dependence of close-encounter yields[34]. The quantal calculations are based on the many-beam description, reviewed in Ch. II, which was seen to describe the experimental results fairly well, at least for planes. From such calculations, also the transverse energy levels are determined, and first we shall compare the number of bound states with the semiclassical estimates.

Bound states. The transverse energy levels for electrons and positrons moving along a {110} plane in silicon are shown in Fig. IV.2, as functions of projectile energy. Zero on the ordinate scale corresponds to a transverse energy equal to the potential maximum (cf. Fig. IV.1). The levels are shown for incidence parallel to the plane as well as for an indidence angle equal to the Bragg angle. For negative transverse energy, corresponding to a bound state, the levels become independent of incidence angle because the components of the wave function belonging to different planar channels no longer communicate. Owing to the difference in shape of the potentials (cf. Fig. IV.1), this happens more rapidly with decreasing transverse energy for electrons than for positrons.

In Fig. IV.3, the number of bound states is shown compared to the estimates, Eqs. (IV.3) and (IV.4), derived in the previous section. Also shown in the figure are results obtained for electrons moving along a ⟨111⟩ axis, compared to the estimate in Eq. (IV.10). For this axis, the many-beam calculations were in Sec. II.7 shown to converge reasonably well with number of beams for an electron energy of 0.7 MeV, but for higher energies, the convergence is more doubtful, and the number of bound states may be slightly underestimated. In any case, the agreement is quite good for the axial as well as for the planar cases, considering the approximate nature of the semiclassical estimates. In particular, the predicted differences in both absolute magnitude and energy dependence are clearly confirmed.

Close-encounter yield. For the comparison between calculations of the yield of a close-encounter process such as large-angle scattering, we concentrate on the planar case. First, the many-beam calculation is technically simpler and more reliable in this case, owing to the rapid convergence with

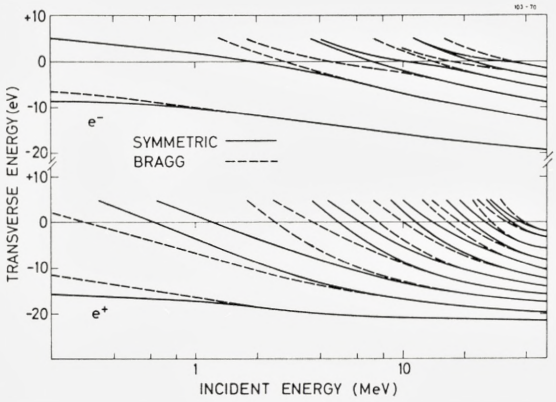

Fig. IV.2: Transverse energy levels for $e-$ and $e+$ incident along a $\{110\}$ plane in Si, as a function of projectile energy. The results are obtained from 20-beam calculations with a thermally averaged (Eq. (III.17)) Molière potential[41]. The levels indicated by solid and dashed curves are obtained for projectile incidence parallel to the plane and at the Bragg angle, respectively. Zero on the ordinate scales corresponds to the maximum of the Molière planar potentials (similar to the potential shown in Fig. IV.1).

number of beams. Second, the classical limit is less well-defined in the axial case, at least for electrons. The classical result derived in the Appendix is based on statistical equilibrium on an energy shell in transverse phase space. In the planar case, this assumption simply leads to results corresponding to an average over depth of penetration, and it is equivalent to the assumption in the quantal calculation of random relative phases of eigenfunctions. For axial channeling, the assumption is based on more subtle arguments, as discussed in the Appendix.

Results for planar channeling of electrons and positrons along a $\{110\}$ plane in silicon are shown in Figs. IV.4 and IV.5. A rapid convergence towards the classical result is indicated, but in contrast to the expectation based on the number of bound states shown in Fig. IV.3, the classical results seem to be somewhat more accurate for electrons than for positrons. In particular is the interference structure at Bragg angles considerably stronger for positrons. This may, however, not be so surprising when we consider the

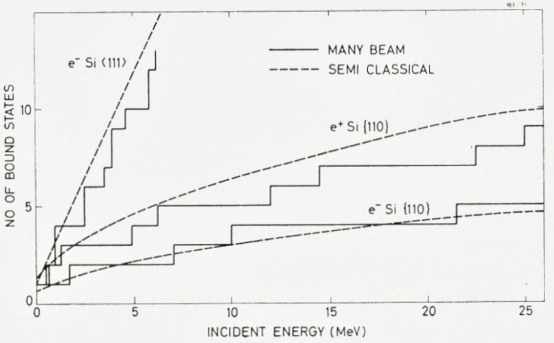

Fig. IV.3: Comparison of the number of bound states derived from Fig. IV.2 with the semiclassical estimates (Eqs. (IV.3) and (IV.4). Also shown are results for a $\langle 111 \rangle$ axis derived from a 60-beam calculation and compared to Eq. (IV.10).

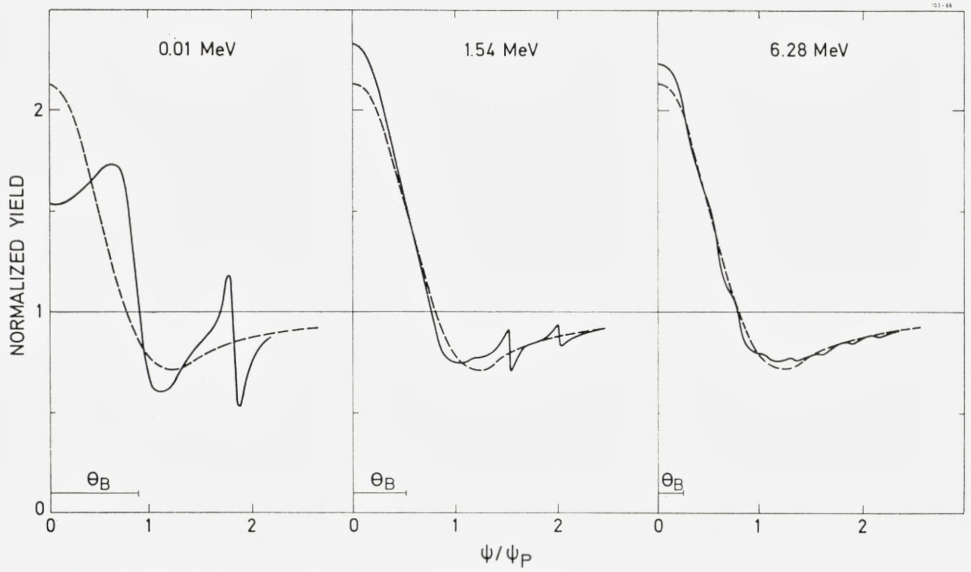

Fig. IV.4: Comparison of classical and quantal calculations of the peak in large-angle-scattering yield for electrons incident on Si along a {110} plane. The classical yield is derived from formulas analogous to those given in Ref. 29 for positive particles, with a thermally averaged Molière planar potential[41], including the contributions from the neighbouring plane (cf. Fig. IV.1). The quantal result is obtained from a 20-beam calculation (Eq. (II.23)), also with the Molière potential and including effects of thermal vibrations (Eqs. (II.15) and (II.17)). The classical result scales with the planar characteristic angle $\psi_p = \psi_1(\mathrm{Ca}/d)^{1/2}$, where d is defined through $Nd^2dp = 1$ (Ref. 29). For each projectile energy, the magnitude of the Bragg angle θ_B is indicated (classical calculations: dashed curves; quantal calculations: solid curves).

fact that the close-encounter yield is proportional to the intensity of the transverse wave function at the atomic positions. For negative projectiles, lattice atoms are situated in a potential minimum, while for positive particles they are at potential maximum. In the latter case, the results therefore depend on the intensity of wave functions close to or inside classically forbidden regions, where the strongest deviations from classical behaviour occur. (Note also that for silicon, the difference in number of bound states between e^+ and e^- is small (cf. Table IV.I).

In spite of the difficulties for axes mentioned above, it may be of interest to compare the quantal and classical calculations also for this case. A set of calculations for electrons incident along a ⟨111⟩ axis is shown in Fig. IV.6. At the higher energies, the agreement is, in fact, rather good. It should be noted that neither of the calculations need correspond very closely to reality. The neglect of inelastic scattering is for axial channeling of negative par-

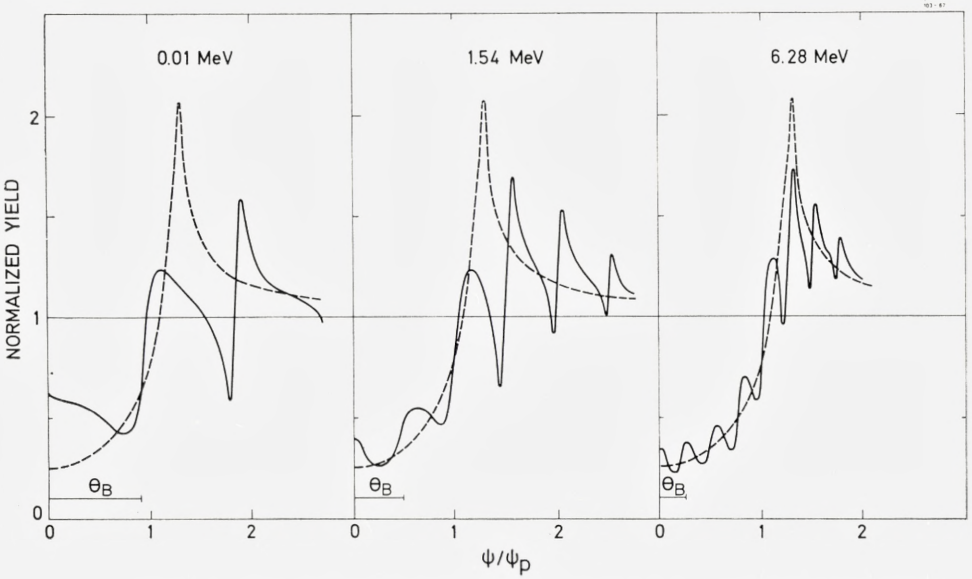

Fig. IV.5: Comparison of quantal (solid curves) and classical (dashed curves) results for positronss incident along {110} plane in Si. For details of the calculations, see Fig. IV.4.

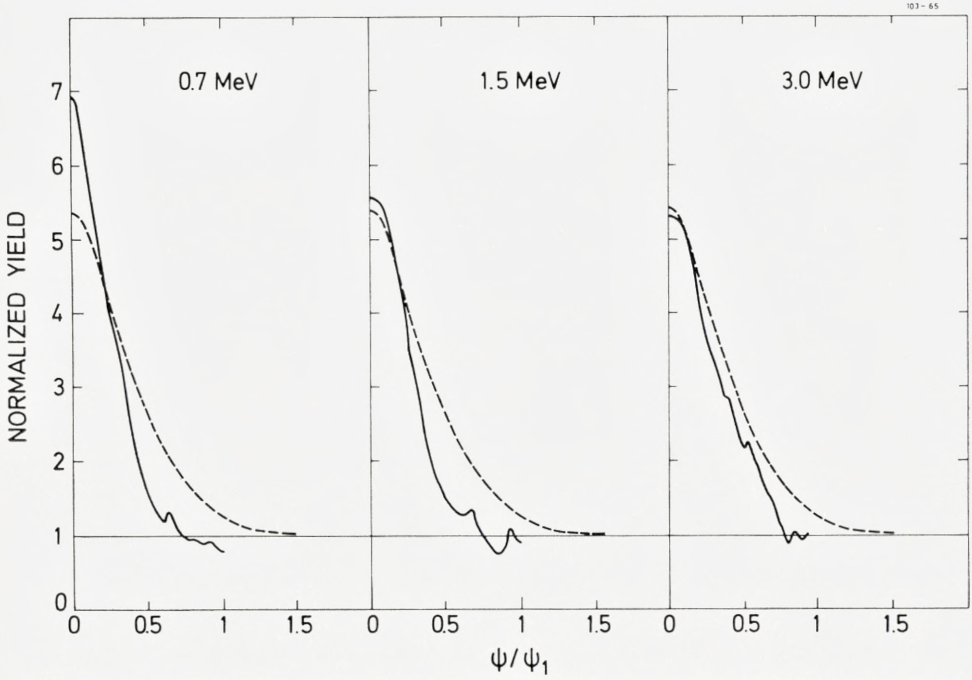

Fig. IV.6: Axial peaks in large-angle-scattering yield for elctrons incident along a ⟨111⟩ direction in Si. Quantal results obtained from 60-beam calculations with Molière potential (formula analogous to Eq. (II.23)) (solid curves). Classical results derived in the Appendix (Eq. (A21)), with the standard potential (Eq. (IV.8)) (dashed curves).

ticles hardly justified even at rather shallow depths since the collisional broadening of closely bound states will be very large. But a statistical treatment is obviously much simplified if classical concepts may be applied, and this should be justified when the volume in phase-space available to bound particles is large enough to correspond to many quantum states.

Finally, for axial channeling of positive particles, the number of "bound" states is very large (cf. Eq. (IV.14) and Table IV.1), and therefore the number of beams needed in a many-beam calculation becomes prohibitively large. However, a comparison of experimental results for positrons and protons indicates[8, 9] that for this case, a classical treatment should be justified.

Acknowledgements

For inspiration and guidance through many discussions, we would like to express our gratitude to J. LINDHARD. Also the collaboration and discussions with E. BONDERUP, A. HOWIE, and E. UGGERHØJ, on problems related to the present work, have been of great value. A special thank to W. L. BROWN for providing excellent working conditions in his laboratory during the time when the experimental part of this work was completed.

Appendix: Classical Estimate for Axial Electron Channeling

In this appendix we shall derive the expression for the axial peak in yield for negative particles, which was used in Chapter IV for comparison with results from "many-beam" calculations. The calculation is based on a classical description of the particle motion. The transverse energy of the particles is assumed to be conserved, and for fixed transverse energy, their trajectories are assumed to fill out the transverse four-dimensional phase-space uniformly. We shall not discuss the validity of these assumptions in detail, but to put the results in perspective it may be useful to review briefly the situation for channeling of positive particles, which has been studied much more thoroughly.

Conservation of transverse energy for channeled particles is the basis of the channeling phenomenon and was discussed in detail by LINDHARD[5]. At large depths of penetration, the distribution in transverse energy is modified due to multiple scattering by electrons and by the small lattice irregularities introduced by the thermal motion of lattice atoms. The effect of these "dechanneling" processes may be calculated with reasonable accuracy from a diffusion equation[5, 42, 43].

Statistical equilibrium, on the other hand, will be established only after a finite depth of penetration. The trend towards equilibrium was studied by LINDHARD[5]. It was shown that when strings are assumed to be randomly distributed in the transverse plane, scattering of the channeled particles by these strings leads to a rapid approach towards equilibrium in transverse-momentum space, the characteristic length being much shorter than that corresponding to dechanneling. At smaller depths, results based on equilibrium may often be interpreted as corresponding to simple averages over azimuthal angle of incidence with respect to a string, and averages over oscillations with depth. As emphasized mainly by BARRETT[44, 45], such an interpretation may not hold in special cases, for example, for the yield of close-encounter reactions for incidence parallel to a string, which at small

depths is higher than estimated from equilibrium by an average factor of 2 to 3. This is a consequence of the regular lattice arrangement of strings, which introduces additional approximately conserved quantities, namely transverse energy with respect to planes (or strings of strings[5]). This will hinder the approach towards equilibrium. A treatment in terms of equilibrium in restricted regions of phase space seems, however, straightforward but has not yet been carried out in detail[46].

Thus for positive particles, the approximations of conservation of transverse energy and statistical equilibrium are consistent and provide a good starting point for a treatment of channeling phenomena. Deviations from these assumptions may then be treated as corrections to the basic picture. For negative particles, however, the situation is less clear. First, multiple scattering is stronger than for positive particles since the atomic scattering centers are situated at a minimum of the transverse potential. Second, the peak in yield is largely due to particles bound in an axial-potential minimum. Such particles interact with only one string, and since the potential is nearly symmetric around the string, angular momentum with respect to this string will be approximately conserved (Rosette motion[47]). Multiple scattering may, however, be strong enough to provide a trend towards equilibrium. In fact, the scattering is strong enough to make the description of the most strongly bound states somewhat uncertain. In the following we disregard these problems and base our treatment upon conservation of transverse energy and statistical equilibrium. The calculations can at least serve as an illustration of the classical treatment, which was discussed in Sec. III.2 and may, as for positive particles, provide a useful standard for comparison, also of experimental results[6, 13] (see also Fig. I.6).

Emission

The derivation is analogous to that in Ref. 5 of the dip in yield for positive particles in the continuum approximation. We use the same notation and also consider emission of particles from a lattice atom, i.e., blocking rather than channeling. The two cases are related by reversibility[5] or reciprocity[7]. If electrons with momentum p and velocity v are emitted isotropically from an atom at a distance r from a string, their distribution in transverse energy, $E_\perp$, is given by

$$\pi(E_\perp, r) = \int d(E\varphi^2)\,\delta(E_\perp - U(r) - E\varphi^2) = \begin{cases} 1 \text{ for } E_\perp > U(r) \\ 0 \text{ for } E_\perp < U(r) \end{cases}. \qquad \text{(A1)}$$

Here, $E = 1/2\ pv = 1/2\ Mv^2$, where M is the relativistic mass (cf. Ch. II). The angle with the string is denoted φ so that $E\varphi^2$ is the transverse kinetic energy. The transverse potential energy is determined by the average string potential $U(r)$. In the following calculations, we once more apply LINDHARD's standard potential,

$$U(r) = -\tfrac{1}{2}E\psi_1^2 \log\left(\left(\frac{Ca}{r}\right)^2 + 1\right), \tag{A2}$$

where ψ_1 is the characteristic angle for axial channeling (Eq. (IV.13)), a the screening distance, and $C \simeq \sqrt{3}$.

The probability of different displacements r is determined by thermal vibrations and denoted $dP(r)$. For the distribution in transverse energy averaged over displacements, we obtain

$$\pi(E_\perp) = \int dP(r) \int d(E\varphi^2)\delta(E_\perp - U(r) - E\varphi^2) = \int dP(r)\Big|_{U(r)<E_\perp}. \tag{A3}$$

By inserting into this formula the standard potential and a Gaussian displacement distribution, LINDHARD obtained a simple analytical estimate of the dip in yield for positive particles.

Surface transmission

When the emitted particles pass the crystal surface, the transverse potential energy is lost and the angle ψ with the string after transmission is determined by $E\psi^2 = E_\perp - U(r)$. For the distribution in angle outside the crystal, we may write

$$P(E\psi^2) = \int dE_\perp T(E_\perp, E\psi^2)\pi(E_\perp), \tag{A4}$$

where $T(E_\perp, E\psi^2)d(E\psi^2)$ is the probability for a particle with transverse energy $E_\perp$ in the crystal to leave the surface at an angle ψ to the string. This probability is determined by the spatial probability density of particles with transverse energy $E_\perp$. In statistical equilibrium, the density in two dimensions is uniform in the allowed area, and we obtain

$$T(E_\perp, E\psi^2) = \int_0^{r_0^2} \frac{d(r^2)}{\hat{r}^2(E_\perp)}\,\delta(E\psi^2 - E_\perp + U(r)). \tag{A5}$$

Here we have, as usual, approximated the area per string in the transverse plane by a circular disc of radius r_0, related to the spacing d of atoms in the string through $\pi r_0^2 = (Nd)^{-1}$, where N is the density of atoms in the crystal. The radius $\hat{r}$ of the accessible area is given by

$$\left.\begin{aligned} U(\hat{r}) &= E_\perp \quad \text{for} \quad E_\perp < U(r_0) \\ \hat{r} &= r_0 \quad \text{for} \quad E_\perp > U(r_0) \end{aligned}\right\} \tag{A6}$$

By combining (A4) and (A5), we obtain

$$P(E\psi^2) = \int_0^{r_0^2} \frac{d(r^2)}{\hat{r}^2(E\psi^2 + U(r))}\, \pi(E\psi^2 + U(r)). \tag{A7}$$

While for positive particles the difference between the distributions $P(E\psi^2)$ and $\pi(E_\perp)$ implied by (A7) is important for $E\psi^2 \sim 0$ only[29], the surface transmission is of major importance for negative particles. The two distributions are completely different. The function $\pi(E_\perp)$ defined by (A3) is below unity for all values of $E_\perp$ and has a tail stretching to $E_\perp \to -\infty$, while P is only defined for $E\psi^2 > 0$ and has a strong increase above unity at $E\psi^2 \simeq 0$. This peak contains the particles which inside the crystal have negative transverse energy, i.e., which are bound in the string potential.

Inserting into (A7) the emission distribution (A3), we obtain

$$\left.\begin{aligned} P(E\psi^2) &= \int_0^{r_0^2} \frac{d(r^2)}{\hat{r}^2(E\psi^2 + U(r))} \int dP(r') \Big|_{U(r') < E\psi^2 + U(r)} = \\ &= \int_0^{r_0^2} \frac{d(r^2)}{r_0^2} \frac{r_0^2}{\hat{r}^2(E\psi^2 + U(r))} \int_0^{\hat{r}} dP(r'). \end{aligned}\right\} \tag{A8}$$

From this expression it is seen that $P \geq 1$. Thus the peak in yield at small angles ψ is not compensated for by a descrease below unity at larger angles. This lack of compensation is a characteristic feature of the continuum string approximation[5]. In the refined treatment by halfway planes, negative 'shoulders' stretching out to angles $\sim 2a/d$ compensate for the excess yield at small angles.

Peak height

From formula (A8), we may calculate the peak height $P(0)$,

$$P(0) = \int_0^{r_0^2} \frac{d(r^2)}{r^2} \int_0^{r} dP(r'). \tag{A9}$$

By inserting a Gaussian distribution,

$$dP(r') = e^{-r'^2/\varrho^2} \frac{d(r'^2)}{\varrho^2}, \quad \varrho \ll r_0, \tag{A10}$$

we obtain by partial integration

$$P(0) \simeq \int_0^{r_0^2} e^{-r^2/\varrho^2} \log\left(\frac{r_0^2}{r^2}\right) \frac{d(r^2)}{\varrho^2} = \log\left(\gamma \frac{r^2}{\varrho^2}\right), \tag{A11}$$

where γ is Euler's constant, $\gamma = 1.78$. This estimate may be compared to the corresponding estimate in Ref. 11 for the standard potential with a cut-off,

$$U(r) = \begin{cases} -E\psi_1^2 \log \dfrac{Ca}{r}, & r < Ca \\ 0 \quad , & r > Ca \end{cases}, \tag{A12}$$

leading to

$$P(0) \simeq 1 + \log\left(\frac{(Ca)^2\gamma}{\varrho^2}\right) \quad \text{for} \quad Ca \gg \varrho. \tag{A13}$$

While (A11) leads to $P(0) \sim 5$–6, formula (A13) predicts a value of $P(0) \sim 2$–3. Since the potential decreases very rapidly and is essentially flat at large distances, the implicit assumption in the derivation of (A11) of an attractive potential at all distances r may not be valid at distances $r \sim r_0$. The cut-off at $r = Ca$ in the potential (A12), however, is probably at too small a distance Thus the two values may reasonably be regarded as upper and lower limits, respectively.

Angular dependence

With the potential (A12) it is easily seen that the excess yield in (A13) is multiplied by a factor $\exp(-2E\psi^2/E\psi_1^2)$ for particles incident at an angle ψ to the string,

$$P(E\psi^2) \simeq 1 + e^{-2E\psi^2/(E\psi_1^2)} \log\left(\frac{(Ca)^2\gamma}{\varrho^2}\right) \quad \text{for} \quad Ca \gg \varrho \tag{A14}$$

as given in Ref. 11.

In order to obtain a reasonably simple analytical estimate with the standard potential (A2), we replace the Gaussian displacement distribution (A10) by

$$dP(r') = \begin{cases} \dfrac{d(r'^2)}{\varrho_0^2}, & r' < \varrho_0 \\ 0 \quad , & r' > \varrho_0 \end{cases}. \tag{A15}$$

Inserting this distribution into (A9), we obtain for the peak height

$$P(0) = 1 + \log \frac{r_0^2}{\varrho_0^2}. \tag{A16}$$

In order to reproduce the result (A11), we choose

$$\varrho_0^2 = \varrho^2 \cdot \frac{e}{\gamma} = 1.53\varrho^2. \tag{A17}$$

With the distribution (A15), the integration in (A8) is straightforward,

$$P(E\psi^2) = \int_0^{r_1^2} \frac{d(r^2)}{\varrho_0^2} + \int_{r_1^2}^{r_2^2} \frac{d(r^2)}{\hat{r}^2(E\psi^2 + U(r))} + \int_{r_2^2}^{r_0^2} \frac{d(r^2)}{r_0^2}. \tag{A18}$$

where r_1 and r_2 are determined by

$$\left.\begin{aligned} U(r_1) &= U(\varrho_0) - E\psi^2 \\ U(r_2) &= U(r_0) - E\psi^2. \end{aligned}\right\} \tag{A19}$$

The two first terms correspond to bound particles with a maximum distance to the string not exceeding ϱ_0 and r_0, respectively, while the third term corresponds to unbound particles. All integrations are elementary, and we obtain,

$$P(E\psi^2) = 1 + e^{-2\psi^2/\psi_1^2} \log(r_2^2/r_1^2) \tag{A20}$$

or inserting the value (A19) for r_1 and r_2,

$$P(E\psi^2) = 1 + e^{-2\psi^2/\psi_1^2} \log \left\{ (r_0^2/\varrho_0^2) \frac{[(Ca)^2 + \varrho_0^2]\, e^{2\psi^2/\psi_1^2} - \varrho_0^2}{[(Ca)^2 + r_0^2]\, e^{2\psi^2/\psi_1^2} - r_0^2} \right\}. \tag{A21}$$

This formula is rather similar to (A14) for not too small angles. As might be expected, however, the inclusion of the outer shallow part of the potential leads to a steep increase in yield at small angles. In fact, the peak height is larger by a factor of ~ 2, and the full width at half maximum is therefore significantly smaller than the value $\Delta\psi = \sqrt{2 \log 2}\ \psi_1$ derived from Eq. (A14).

References

1) E. Bøgh, J. A. Davies, and K. O. Nielsen, Phys. Letters **12**, 129 (1964).
2) B. Domeij and K. Björkqvist, Phys. Letters **14**, 127 (1965).
3) G. Astner, I. Bergström, B. Domeij, L. Eriksson, and A. Persson, Phys. Letters, **14**, 308 (1965).
4) E. Uggerhøj, Phys. Letters **22**, 382 (1966).
5) J. Lindhard, Mat.-Fys. Medd. Dan. Vid. Selsk. **34**, No 14 (1965).
6) E. Uggerhøj and J. U. Andersen, Can. J. Phys. **46**, 543 (1968).
7) M. von Laue, Materiewellen und Ihre Interferenzen (Akademische Verlagsgesellschaft, Leipzig, 1948).
8) J. U. Andersen, W. M. Augustyniak, and E. Uggerhøj, Phys. Rev. **B3**, 705 (1971).
9) M. J. Pedersen, J. U. Andersen, and W. M. Augustyniak, Rad. Effects **12**, 47 (1972).
10) P. Lervig, J. Lindhard, and V. Nielsen, Nucl. Phys. **A96**, 481 (1967).
11) J. Lindhard, Atomic Collision Phenomena in Solids (North Holland Publishing Co., Amsterdam, 1970), p. 1.
12) E. Uggerhøj and F. Frandsen, Phys. Rev. **B2**, 582 (1970).
13) S. Kjær Andersen, F. Bell, F. Frandsen, and E. Uggerhøj, Phys. Rev. **B8**, 4913 (1973).
14) P. B. Hirsch, A. Howie, R. B. Nicholson, D. W. Pashley, and M. J. Whelan, Electron Microscopy of Thin Crystals (Butterworths, 1965); se also A. Howie in *Modern Diffraction and Imaging Tcehniques in Materials Science* (North-Holland, Amsterdam 1970), p. 295.
15) P. B. Hirsch, A. Howie, and M. J. Whelan, Phil. Mag. **7**, 2095 (1962).
16) P. Duncomb, Phil. Mag. **7**, 2101 (1962).
17) C. R. Hall, Proc. Roy. Soc. **A295**, 140 (1966).
18) A. Howie, M. S. Spring, and P. N. Tomlinson, Atomic Collision Phenomena in Solids (North Holland Publishing Company, Amsterdam, 1970), p. 34; see also P. N. Tomlinson and A. Howie, Phys. Letters **27 A**, 491 (1968).
19) M. J. Whelan, Atomic Collision Phenomena in Solids (North-Holland Publishing Company, Amsterdam, 1970), p. 3.
20) A. Howie, Phil. Mag. **14** 223 (1966), and Brookhaven National Laboratory, Report No 50083, Solid State Physics with Accelerators (1967) p. 15.
21) R. E. De Wames and W. F. Hall, Acta Cryst. **A24**, 206 (1968).
22) R. E. De Wames, W. F. Hall, and G. W. Lehmann, Phys. Rev. **174**, 392 (1968).
23) L. T. Chadderton, Phil. Mag. **18**, 1017 (1968).

24) L. T. Chadderton, J. Appl. Cryst. **3**, 429 (1970).
25) M. V. Berry, J. Phys. **C 4**, 697 (1971).
26) M. V. Berry, Rad. Effects **27**, 1 (1973).
27) D. S. Gemmel, Rev. Mod. Phys. **46**, 129 (1974).
28) L. T. Chadderton in *Channeling*, ed. D. V. Morgan (Wiley, N. Y. 1973).
29) J. U. Andersen, Mat. Fys. Medd. Dan. Vid. Selsk. **36** No. 7 (1967), J. U. Andersen and L. C. Feldman, Phys. Rev. **B1**, 2063 (1970).
30) J. U. Andersen, J. A. Davies, K. O. Nielsen, and S. L. Andersen, Nucl. Instr. Methods **38**, 210 (1965).
31) N. Bohr, Mat.-Fys. Medd. Dan. Vid. Selsk. **18** No 8 (1948).
32) E. Keil, E. Zeitler, and W. Zinn, Z. Naturforsch. **15a**, 1031 (1960).
33) F. Fujimoto, S. Takagi, K. Komaki, H. Koike, and Y. Uchida, Rad. Effects **12**, 153 (1972).
34) S. Kjær Andersen, Thesis, University of Aarhus (1974).
35) A. Howie and R. M. Stern, Z. Naturforschung **27a**, 382 (1972).
36) J. P. Spencer, C. J. Humphreys, and P. B. Hirsch, Phil. Mag. **26**, 193 (1972).
37) Y. Kagan and Y. V. Kononets, Zh. Edsp. Teor. Fiz. **58**, 226 (1970). [Sov. Phys. -JETP **31**, 124 (1970)].
38) C. J. Humphreys and P. B. Hirsch, Phil. Mag. **18**, 115 (1968).
39) D. Cherns, A. Howie, and M. H. Jacobs, Z. Naturforsch. **28a**, 565 (1973).
40) D. Bohm, *Quantum Theory* (Prentice-Hall, N. Y. 1951)
41) B. R. Appleton, C. Erginsoy, and W. M. Gibson, Phys. Rev. **161**, 330 (1967).
42) E. Bonderup, H. Esbensen, J. U. Andersen, and H. E. Schiøtt, Rad. Effects **12**, 261 (1972).
43) H. E. Schiøtt, E. Bonderup, J. U. Andersen, H. Esbensen, M. J. Pedersen, D. J. Elliott, and E. Lægsgaard, in Proc. 5th Conf. on Atomic Collisions in Solids, Gatlinburg, Tenn., Vol. 2, p. 843 (1973).
44) J. H. Barrett, Phys. Rev. **166**, 219 (1968).
45) J. H. Barrett, Phys. Rev. Letters **31**, 1542 (1973).
46) J. A. Golovchenko, Phys. Rev. **B 13**, 4672 (1976).
47) H. Kumm, F. Bell, R. Sizmann. and H. J. Kreiner, Rad. Effects **12**, 53 (1972).

Indleveret til Selskabet august 1976.
Færdig fra trykkeriet september 1977.